A quantitative analysis of double-sided surface waviness on TEHL line contacts

P. Havaej [a], J. Degroote [b, c], D. Fauconnier [a, c*]

[a] *Soete Laboratory, Department of Electromechanical, Systems & Metal Engineering, Faculty of Engineering and Architecture, Ghent University, Technologiepark 46, 9052 Zwijnaarde, Belgium*

[b] *STFES, Department of Electromechanical, Systems & Metal Engineering, Faculty of Engineering and Architecture, Ghent University, Sint-Pietersnieuwstraat 41, 9000 Ghent, Belgium*

[c] *Flanders Make @ UGent – Core Lab EEDT-MP*

Abstract

In this paper, the effects of double-sided surface waviness on Thermo-Elastohydrodynamic Lubrication (TEHL) in line contacts are investigated deterministically through numerical simulations. The effects of surface amplitude, wavelength, relative position, and slide-to-roll ratio have been studied. The classic approach, which consists of an equivalent deformable body with superimposed surface waviness, is critically evaluated and compared to results from full two-body simulations. Under the investigated conditions, the equivalent and two-body approaches show about 17%, 21%, and 26% deviations in maximum pressure, temperature, and friction, respectively. It is demonstrated that the fundamental cause of the observed deviations, which results in a phase shift that cannot be described by the equivalent geometry, is the tangential elastic deformation of surface asperities.

Keywords: Thermo-Elastohydrodynamic Lubrication (TEHL), Computational Fluid Dynamics (CFD), Surface waviness**,** Equivalent Geometry

[*] Corresponding author. Address: Department of Electromechanical, Systems and Metal Engineering, Faculty of Engineering and Architecture, Ghent University, Ghent, Belgium. Emails: dieter.fauconnier@ugent.be

1. Introduction

Adequate lubrication of mechanical machine components ideally implies full or partial separation of the opposing surfaces by a thin lubricant film, minimizing frictional losses, damage, wear as well as noise and vibration. Besides the load transfer at the contact, the lubricant film must be able to evacuate the frictional heat from the contact area, as well as contaminants and wear debris. In non-conformal contacts, representative for bearings and meshing gears, the so-called Elasto-Hydrodynamic Lubrication (EHL) regime ideally prevails. EHL is characterized by very thin lubricant films (50 nm – 1 μm), locally extreme hydrodynamic pressures (up to $1 - 4$ GPa), and corresponding local elastic deformation of the solid surfaces. The lubricant film is able to sustain these pressures and transfer the high loads due to the compressibility and piezo-viscous behaviour of the lubricant, which manifests in a rise of the lubricant viscosity by several orders of magnitude. Thermal aspects become important in the case of high contact loads, high entrainment velocities and non-zero slide-to-roll ratios. Indeed, besides compressive heating in EHL contacts, shear heating plays a major role in the case of high local slip-to-roll ratios, affecting, to a great extent, the viscosity and other thermomechanical properties. This is commonly denoted as Thermo-Elastohydrodynamic Lubrication (TEHL).

A clear quantitative understanding of the effects of surface topography and surface roughness on TEHL is highly desirable to better predict the role of the surface finishing of mechanical components on the local contact conditions, i.e. pressure, temperature and film thickness, and subsequently, the service life of mechanical components. Since, for typical TEHL conditions, the film thickness is in the order of the surface roughness, it is clear that the slightest distortion - even in the order of tens of nanometres - can affect the lubrication in the contact [1]. Besides local pressure variations, shear heating and the lubricant temperature are heavily influenced by the surface topography [2].

In literature, different approaches have been adopted to take surface roughness effects into account. Table 1 gives a condensed summary of the international academic state-of-the-art, with a focus on TEHL modelling and surface topography. Two classes can be distinguished, i.e. deterministic models and stochastic models. In each class, different solution methods have been opted for.

Table 1 Literature review on modelling of surface topography effects in TEHL contacts, (L): line contacts, Point contacts (P).

	Deterministic models		**Stochastic Models**
	Sinusoidal topography	**Realistic topography/roughness**	
Iso-thermal +Reynolds +Boussinesq	He et al. [3], 2014, (P) Hu and Zhu [4], 2000, (P) Kweh et al. [5], 1992, (L) Lubrecht et al. [6], 1988, (L)	Liu et al. [7], 2017, (L) Ren et al [8], 2009, (L) Venner and Napel [9], 1992, (L) Zhu and Ai [10], 1997, (P)	Kim et al. [11], 2008 Morales-Espejel [12], 2009 Pei et al. [13], 2020, (L) Yan et al. [14], 2014, (P)
Reynolds +Boussinesq +Temperature	Allen and Raeymaekers [15] Hooke et al. [16,17] 2019, (L) Hultqvist [18], 2020, (L) Kaneta et al. [19–21] 2020, (P)	Chimanpure et al. [22] Everitt et al. [23,24], 2020, (L) Mariana et al. [25], 2019, (P) Xu and Sadeghi [26], 1996, (P) Yong et al. [27], 2019, (L) Shi et al. [28] 2016, (P) Zhao et al. [29], 2020 (P)	Masjedi and Khonsari [30], 2014, (L) Meng et al. [31], 2008 Wang et al. [32], 2017, (P) Gu et al. [33], 2016, (L)
Navier-Stokes +Boussinesq +Temperature	-	Srirattayawong [34] (P)	-
Navier-Stokes +Linear Elastic +Temperature	Hajishafiee [35] (L)	-	-

The most conventional stochastic approach to studying EHL rough contact problems utilizes so-called flow factors in the Reynolds equation to account for the presence of asperities and the subsequent flow blockage. This method, proposed by Patir & Cheng [36], is based on the average flow model and omits crossflow interactions. The asperities distribution in such a stochastic approach may be Gaussian or not [28]. In a different approach, initially introduced by Hook [37], perturbation analysis was used. Hook considered that the transient solution of a moving roughness has two parts: (i) the particular integral, i.e., steady-state solution of the problem, and (ii) a complementary function. While the Reynolds equation is employed in the particular integral, the second part of the roughness solution is solved by means of a perturbation analysis. In spite of stochastic and average flow models, a deterministic approach and numerical modelling of TEHL contacts can describe both global and local pressure, lubricant film, and thermal behaviour in more fundamental detail [38]. However, this comes at higher computational costs and possibly the need for high-performance computing.

Low amplitude rough surfaces were studied by Hooke [39–41]. He investigated the elastic-piezo-viscous lubrication regime and non-Newtonian behaviour in EHL for the case where asperities are travelling through the EHL contact. Hooke reported that surface profile variations inevitably increase pressures and temperatures in contact and decrease film thickness [17]. Mariana et al. [25] experimentally and numerically studied the surface textures in the point contact at isothermal conditions without non-Newtonian effects. They showed that the relative position of the surface features with respect to the countersurface significantly influences the friction forces and wear behaviour. Srirattayawong [34] used the CFD-Boussinesq approach and reported that the skewness has a larger influence on the pressure profile in the contact width, and when kurtosis is lower than 3, the average lubricant film is comparable to the smooth contact film thickness. In previous studies, the equivalent geometry has been assumed, in which the undeformed equivalent surface profile is the superposition of both opposing profiles.

In most of the investigations of surface waviness or roughness effects on TEHL conditions, the equivalent geometry in half-space has been used, where the superposition of the surface profiles has been imposed on the deformable surface as equivalent surface waviness/roughness. The majority of these studies also used the Boussinesq integral to describe the normal deformation of surface asperities, although a linear elastic solver could also describe the solid deformation. Only a few studies have explicitly considered a two-body geometry without relying on the equivalent half-space assumption. Habchi [42] emphasized the limitations of using the half-space theory and Boussinesq integral in the presence of surface features by identifying three significant shortcomings for modelling asperity deformation. The first shortcoming is that this approach assumes that the deformation due to the contact pressure acts only in the vertical direction, disregarding potential displacements in other directions. The second drawback is that it employs equivalent solid properties that are not suitable for scenarios with surface features. Finally, the half-space approximation fails to consider the deformation of the surface features themselves. Kaneta et al. [19] studied the effects of the interaction of the transverse and longitudinal waviness profile on TEHL contact through Reynolds solution using the Eyring shear thinning model while assuming constant thermal properties. They reported that the friction is lower when the surface with a longitudinal wavy profile has a lower thermal conductivity than the countersurface. However, the elastic deformation along the flow direction has not been included in this study, implying that the asperities cannot deform tangentially. Recently, Hultqvist et al. [2] evaluated the transient effects of a surface feature passing through a TEHL line contact. They tried to enhance the insight into contact roughness by solving the Reynolds equation and imposing the surface profile on the rolling element. They showed that the lubricant temperature increased extremely under sliding conditions, particularly near the asperity. In addition, they studied the rough, time-dependent TEHL problem with a focus on thermal non-Newtonian effects [18]. They showed that not only the surface feature combination can significantly change the film and pressure profile, but also the relative motion of surfaces asperities in the contact. In their study, the authors made use of the surface profile superposition.

Traditionally, the well-established Reynolds-Boussinesq approach is used to model EHL. It is supplemented with various constitutive equations for the lubricant properties as a function of the state variables to describe compressibility, non-Newtonian shear thinning, piezo-viscosity, as well as the dependency on thermal properties of the lubricant [43,44]. The classic Reynolds equation is obtained by averaging over film thickness and can be considered as a reduced-order model in N-1 dimensions of the N-dimensional Navier-Stokes equations. It has undoubtedly proven its worth in terms of both accuracy and computational efficiency for isothermal EHL [45,46]. On the other hand, TEHL involves compressive and shear heating in the lubricant film, as well as convective and conductive thermal transport through the lubricant film and the solid bodies. Thereto, the N-1-dimensional Reynolds-Boussinesq equations are typically supplemented with an N-dimensional temperature equation which describes thermal transport along and across the lubricant film and the solid bodies. To properly account for the thermally-induced variation of viscosity and density across the film thickness, a modified Reynolds equation should be used [47]. For example, Peiran and Shizhu [48] added a 2D thermal equation to the 1D modified Reynolds-Boussinesq model for obtaining the temperature field along and across the lubricant film.

Although the computational efforts involved in solving the full Navier-Stokes equations for the lubricant and the Navier-Cauchy equations for the solids are significantly higher in comparison with those of the Reynolds-Boussinesq approach, no averaging of thermomechanical properties across the fluid film is required [49], which are important when considering non-smooth surfaces. Moreover, potential inertial effects for both momentum and temperature equations in the in- and outlet domains are handled naturally, as well as gradient effects due to pressure-viscosity behaviour [50]. Indeed, Hao and Meng [51] performed a comparison between Reynolds and CFD-FEM approaches for Newtonian fluid and 3D line contacts. A significant difference in temperature profiles has been observed, which is mainly attributed to the effects of reverse flow, increasing the shear rate at the inlet, and enhancement in heat transfer between contact and inlet region. Furthermore, the CFD approach predicted a much higher pressure spike than Reynolds; its location shifted to the center of the contact as well. The differences between both methods are reported to depend on the entrainment speed, Slide-to-Roll Ratio (SRR), and load. Scurria et al. [46] compared the solutions of Reynolds and Navier-Stokes for EHL contact with isothermal and Newtonian lubricants. They observed that neglecting the inertia term influenced the accuracy of the Reynolds solution at low load and relatively high speeds of rotation [49]. Hartinger et al. [52] performed initial research on using CFD and accurate flow modelling in a 2D line TEHL contact considering thermal, cavitation, compressibility, and shear thinning effects. They found a significant pressure gradient across the lubricant film in sliding conditions, mainly due to the viscosity gradient induced by the temperature gradient across the film thickness. Moreover, a thermal validation of this model for 3D point TEHL contact was presented later [53]. Hajishafiee et al. [54] extended Hartinger's model to include a linear elastic structural model for the solid body as well as a strong and two-way FSI coupling model, which is more appropriate for high load and different rheological laws. Bruyere et al. [55] presented a single-phase CFD model for the lubricant flow and coupled it to a Finite Element solver for the structural part. They studied dimple formation under zero entrainment velocity conditions and obtained interesting results to increase the understanding of heat transfer and the flow pattern in contact, especially in the case of pure sliding, where conductivity in the solid can explain the local friction value.

Enabled by the increasing availability of computational power and motivated by the rising interest in fundamental multi-scale and multi-physics modelling of TEHL, Computational Fluid Dynamics (CFD) has been selected by the authors as the research tool of preference to study surface topography effects. In CFD, the lubricant flow is described by the N-dimensional Navier-Stokes equations, including the temperature equation, in combination with proper constitutive laws for the lubricant properties without averaging. The CFD flow solver can be coupled to a structural solver to describe the elastic deformation of the solid using mostly a Fluid-Structure Interaction (FSI) algorithm.

In this work, we investigate the effect of variable amplitude, wavelength, and phase shift between opposing wave crests on the hydrodynamic pressure, the temperature and heat flux distributions as well as the film thickness, and the coefficient of friction. The latter is a crucial parameter in the interaction between two rough surfaces and contributes to a better understanding of lubricant behaviour when the asperities are sliding above each other. We investigate the influence of the assumption of imposing both surface profiles on a single equivalent body. Thereto, we consider the physical case of two solid cylinders with equal radii of curvature and imposed sinusoidal surface waviness, rolling against each other with different slide-to-roll ratios. Two approaches are followed. In the first approach, 2D TEHL calculations were performed for this line contact, using an equivalent geometry formed by a solid deformable cylinder with an equivalent radius, superimposed waviness profiles and equivalent material properties rolling over a flat rigid surface. In the second approach, 2D TEHL calculations will be performed for the real contact formed by the two deformable solids without assuming any superposition of profiles or surface waviness. The results of both deterministic simulations will be compared and evaluated, and the effect of the underlying assumptions for the equivalent geometry – as often used in literature – will be quantified. For the TEHL calculations, a CFD-FSI modelling approach is opted for in combination with conjugate heat transfer to the solid bodies. Although the asperities are constantly in relative motion to each other in reality, we consider here pseudo-transient calculations, representing instantaneous snapshots in time. The lubricant is also described with the appropriate constitutive models, taking into account all relevant effects.

2. Governing equations

The CFD-FSI approach used in this study consists of fluid flow equations, a linear elastic equation, and an interface coupling algorithm, which are explained in detail in the following sections. This method is applied on 2D lubricated line TEHL contacts.

2.1. Geometry & Computational Domain

A schematic view of the 2D geometry and surface profile of the equivalent geometry with a cylinder over a flat plate is shown in Figure 1-a, and a real geometry with two elastic bodies is presented in Figure 1-b. The fluid is pressurized in the gap, and it makes a clearance between the surfaces. In addition, the surface profile plays an essential role in the lubrication of contacts.

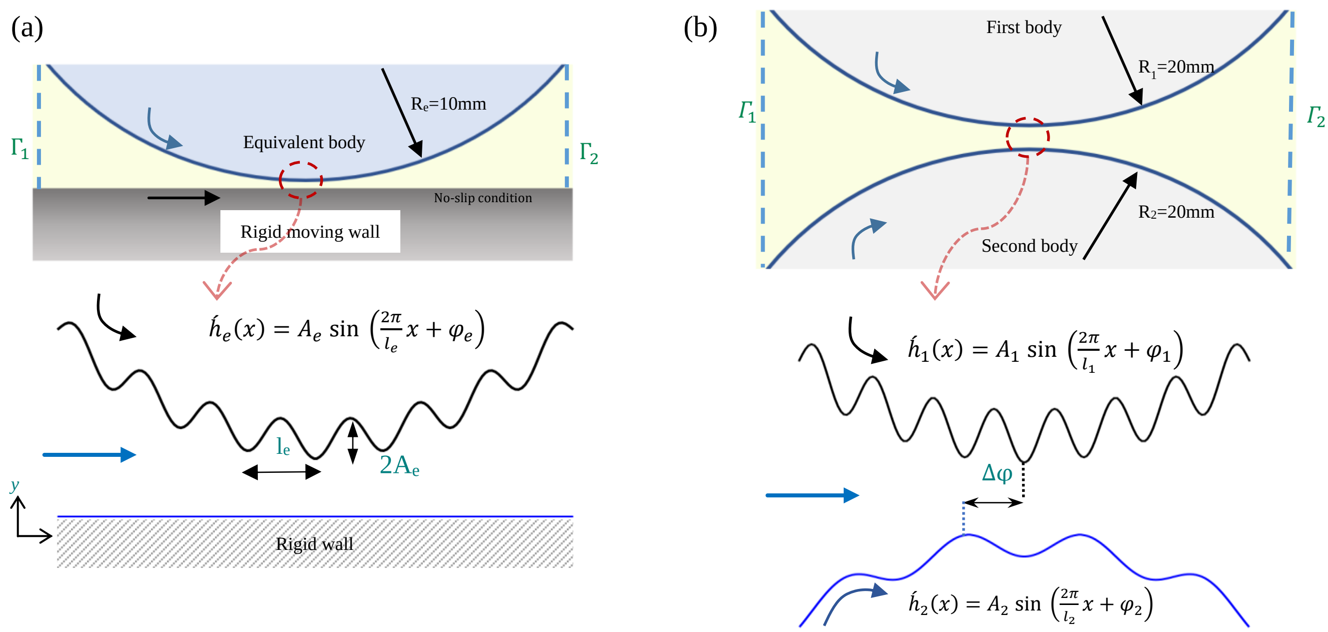

Figure 1 A schematic view of (a) the equivalent geometry and (b) the real geometry.

2.2. Homogenous Equilibrium Model

In the Homogeneous Equilibrium Model (HEM), the lubricant is considered a homogeneous mixture of liquid and vapour, described by a single set of mass and momentum equations. The mass conservation of the lubricant mixture is given by

$$\frac{\partial \rho}{\partial t} + \nabla \cdot (\rho \vec{u}) = 0 \tag{1}$$

in which ρ denotes the density depending on the compressibility, ψ, and pressure. Momentum conservation for the liquid/vapour mixture yields

$$\frac{\partial (\rho \vec{u})}{\partial t} + \nabla \cdot (\rho \vec{u}\vec{u}) + \nabla \cdot \tau = -\nabla \cdot p \tag{2}$$

in which p is pressure τ denotes the viscous stress tensor, given as

$$\tau = -\mu(\nabla \vec{u} + (\nabla \vec{u})^T) + \mu \frac{2}{3} I \nabla \cdot \vec{u} \tag{3}$$

The model of Karrholm and Weller [56] has been used here to describe the cavitating lubricant, combining a homogeneous equilibrium model with a barotropic Equation of State (EoS). Assuming a barotropic description of the lubricant phase change, the equation of state of the liquid-vapour mixture can be written as

$$\frac{D\rho}{Dt} = \psi \frac{Dp}{Dt}. \tag{4}$$

Integration of the separable equation (4) to pressure, taking into account the saturation pressure as a lower boundary, the mixture density is obtained as

$$\rho = \psi\,(p - p_{sat}) + \alpha_l \rho_{l,0} + \left(\alpha_v \psi_v + \alpha_l \psi_{l,M}\right) p_{sat} \tag{5}$$

where α_l and α_v denote the liquid and vapor volume fractions, respectively, defined as

$$\alpha_v = \frac{\rho - \rho_{l,sat}}{\rho_{v,sat} - \rho_{l,sat}} \tag{6}$$

$$\alpha_l = 1 - \alpha_v \tag{7}$$

Here, $\rho_{l,sat}$ and $\rho_{v,sat}$ are the density of the liquid and vapor phases at the saturation pressure. The compressibility of the mixture can be defined by different models [57], but in this work, the following linear relation is assumed

$$\psi = \alpha_v \psi_v + \alpha_l \psi_{l,M} \tag{8}$$

The densities of respectively the vapour and liquid fractions in equation (5) are given by the ideal gas law

$$\rho_v = \psi_v p \tag{9}$$

and a linearized description of the liquid compressibility as

$$\rho_l = \rho_{l,0} + \psi_{l,M} p \tag{10}$$

$$\rho_{l,0} = \rho_{l,sat} - \psi_{l,sat} p_{sat} \tag{11}$$

Here, ψ_v and ψ_l denote the compressibility of vapor and liquid phases, respectively. $\rho_{l,0}$ is the density of the liquid at zero pressure and ψ_v is assumed constant and independent of temperature. For the liquid phase, $\psi_{l,sat}$ and $\psi_{l,M}$ denote the compressibility values at saturation pressure and the average compressibility over the entire pressure range. The latter can be evaluated as

$$\psi_{l,M}(p,T) = \frac{1}{p - p_{sat}} \int_{p_{sat}}^{p} \psi_l(p',T)dp' = \frac{1}{p - p_{sat}} \int_{p_{sat}}^{p} \left(\frac{\partial \rho_l}{\partial p'}\right)_s dp' \tag{12}$$

In which $\rho_l = f(p, T)$ is known.

Although the phase change is primarily governed by a decrease in pressure, hence the name barotropic EoS, temperature effects are included in phase density; hence, the EoS depends on pressure and temperature.

The mixture dynamic viscosity is also assumed to be a weighted average of both phase volume fractions

$$\mu = \alpha_v \mu_v + \alpha_l \mu_l \tag{13}$$

2.3. Temperature equation

Following the work of Hartinger et al. [52,53,58] and Hajishafiee [54,59], the following transport equation for the mixture temperature has been included in the model, i.e.

$$\rho C_p \frac{DT}{Dt} + \frac{D\alpha_v}{Dt}(\rho_v h_v - \rho_l h_l) = \nabla \cdot (k\, \nabla T) - \tau : \nabla \vec{u} + \alpha_v \frac{DP}{Dt} + \alpha_l \beta T \frac{DP}{Dt} \tag{14}$$

Note that the two last terms on the right-hand side in equation (14) is essential to describe compressive heating. A detailed derivation of the energy equation is given in Appendix B.

At Γ_1 (inlet), and Γ_2 (outlet) boundaries of the domain, the static pressure is imposed to be the ambient pressure (Dirichlet), whereas the velocity is calculated according to the mass-flux or velocity field at the neighbouring cells. For the temperature equation at Γ_1 and Γ_2, a hybrid

Dirichlet-Neumann boundary condition is imposed, which locally depends on whether the flow is entering ($u_{n,normal} = \vec{u}_n . \vec{n} > 0$) or leaving ($u_{n,normal} < 0$) the domain in the recirculation zone. Note that a pure Neumann boundary condition is always automatically imposed at the Γ_2 for velocity and temperature due to the flow direction in studied cases.

$$\begin{cases} T = T_0 & u_{n,normal} > 0 \\ \frac{\partial T}{\partial x} = 0 & u_{n,normal} < 0 \end{cases} \tag{15}$$

$$\begin{cases} u_{normal} = \frac{\vec{Q} \, . \, \vec{n}}{\rho \, A \, . \vec{n}} \; , \; u_{tangential} = 0 & u_{n,normal} > 0 \\ \frac{\partial \vec{u}}{\partial n} = 0 \, , \; u_{tangential} = 0 & u_{n,normal} < 0 \end{cases} \tag{16}$$

Where $\vec{Q}$, $\vec{u}_n$ are the mass flux and velocity at the neighbouring cell, respectively. Also, A and $\vec{n}$ are the surface area and normal vector of the boundary face, respectively. There are two velocity components associated with the boundary face: u_{normal} and $u_{tangential}$. In the case of the inflow condition, the tangential component of velocity is zero because the pressure is fixed on this boundary, and there is no pressure gradient in the tangent direction.

At the fluid-solid interfaces, conjugate heat transfer is imposed, implying identical temperatures and heat fluxes at the solid and lubricant boundaries. Also, the tangential velocity at rotating surfaces is implemented as $\vec{u} = \vec{\omega} \times \vec{r}$, where $\vec{\omega}$ is the prescribed rotating speed and $\vec{r}$ is the distance to the center of rotation. Moreover, the normal velocity at walls can be calculated based on structural deformation. Hence, the flow at the wall will move with the wall.

At solid walls, it is worth noting that no-slip boundary conditions are applied for the fluid velocity, whereas Neumann boundary conditions are imposed for the pressure there. For the rigid wall sliding over the contact in the equivalent geometry, the Carslaw-Jaeger temperature boundary condition is applied, which has been recommended for TEHL contacts [60,61], i.e.

$$T_{Cars} = \sqrt{\frac{1}{\pi \rho_s C_s k_s u_s}} \int_{-\infty}^{x} q_f(\hat{x}) \frac{d\hat{x}}{\sqrt{x - \hat{x}}} \tag{17}$$

This boundary can be used for Peclet numbers greater than 5, $Pe = \frac{L_{ch} u_s}{\alpha_T} > 5$, which is fully satisfied in this study. L_{ch}, u_s, and α_T are the characteristic length of the contact, the solid surface speed, and the thermal diffusivity coefficient, respectively.

2.4. Constitutive equations

In this study, Tait's model is used as an equation of state for the liquid phase of the lubricant. This model has shown good agreement with experimental data, especially at high pressures [62]. The dependency of viscosity on pressure and temperature is described by the Doolittle model [63]. Furthermore, the non-Newtonian behaviour of the lubricant is modelled by the modified Carreau model as described by Bair [62]. In this model, a limiting shear stress is assumed in equation (25) to avoid unphysical viscosity values. All constitutive models are presented in Table 2.

Moreover, at a pressure of the orders of magnitude of GPa, the thermal properties are not constant; hence, equations of (26)-(29) include pressure and temperature influences on the heat conductivity and heat capacity of the lubricant [44,64].

Table 2 Constitutive equations.

Description	Equation	
Tait equation of state [62]	$\rho_{Tait} = \rho_R \left(\frac{1}{V_0/V_R} \times \frac{1}{V/V_0} \right)$	(18)
Ratio of the fluid volume at pressure P relative to the volume at ambient pressure	$\frac{V}{V_0} = 1 - \frac{1}{1+\acute{K}_0} ln\left[1 + \frac{P}{K_0}\left(1+\acute{K}_0\right)\right]$	(19)
Bulk modulus at ambient pressure	$K_0 = K_{00} exp^{-\beta KT}$	(20)
The volume of the liquid at ambient pressure relative to the volume at the reference state	$\frac{V_0}{V_R} = 1 + a_V(T - T_R)$	(21)
Doolittle viscosity model for pressure and temperature dependency [63]	$\mu_{Doolittle} = \mu_R \exp\left(B\, R_0 \left(\frac{\frac{V_\infty}{V_{\infty,R}}}{\frac{V}{V_R} - R_0 \frac{V_\infty}{V_{\infty,R}}} - \frac{1}{1-R_0} \right) \right)$	(22)
Relative occupied volume	$\frac{V_\infty}{V_{\infty,R}} = 1 + \varepsilon(T - T_R)$	(23)
Shifted Carreau shear thinning model [62]	$\eta_{Shifted-Carreau}(T, p, \dot{\gamma}) = \mu_{Doolittle}\left[1 + \left(\lambda_R \frac{\tau}{\mu_R} \frac{T_R}{T} \frac{V}{V_R}\right)^2\right]^{(n-1)/2}$	(24)
Limiting shear stress model [65]	$\tau_L = \Lambda\, p$	(25)
Thermal conductivity [44,64]	$\kappa = \frac{V}{V_R}\left(1 + A\left(\frac{T}{T_R}\right)\left(\frac{V}{V_R}\right)^3\right)$	(26)
	$k = C + B\kappa^{-s}$	(27)
Heat capacity [44,64]	$\chi = \left(\frac{T}{T_R}\right)\left(\frac{V}{V_R}\right)^{-4}$	(28)
	$\rho C_P = C_0 + m\chi$	(29)

2.5. Solid model

To calculate stresses and deformations in the solid domain, a linear elastic equation for moderate stresses and strains is employed, as written below [66]:

$$\rho_s \frac{\partial^2(\vec{v})}{\partial t^2} - \nabla \cdot \sigma_s = \rho_s f_b \tag{30}$$

$$\sigma_s = 2\mu_s \varepsilon + \lambda_s tr(\varepsilon) I \tag{31}$$

$$= \mu_s \nabla\vec{v} + \mu_s(\nabla\vec{v})^T + \lambda_s I\big(tr(\nabla\vec{v})\big)$$

$$\mu_s = \frac{E}{2(1+\vartheta)}\ ,\ \lambda_s = \frac{\vartheta E}{(1+\vartheta)(1-2\vartheta)} \tag{32}$$

in which, $\vec{v}$ is the displacement vector, f_b is the body force, I denotes the unit tensor, μ_s and λ_s are Lame’s coefficients. Hooke’s law has been used in the derivation of equation (30) to describe the constitutive behaviour of the linear elastic material.

For the solid domain interface with the fluid, both kinematic and dynamic conditions should be satisfied. The kinematic condition requires that both velocity and displacement are equal on the interface for each face [67].

$$\vec{v}_{f,i} = \vec{v}_{s,i} \, , \vec{u}_{f,i} = \vec{u}_{s,i} \tag{33}$$

Where $\vec{u} = \dot{\vec{v}}$ is the velocity. Also, the dynamic condition can be derived from the principle of linear momentum equation, which results in the equation of force balance at the fluid-solid interface.

$$\sigma_{f,i} = \sigma_{s,i} \tag{34}$$

Shear and pressure forces are included in σ_f.

The displacement vector field is solved along with heat conduction in the moving solid materials, as presented in equation (35).

$$\rho_s C_s \frac{\partial T}{\partial t} + \dot{\vec{v}}.\nabla T = \nabla \cdot (k_s \nabla T) \tag{35}$$

Note that the initial and far-field temperature of solids are the same as the inlet temperature of the lubricant (T_0).

2.6. Load balance

The external load (L_{ext}) exerted on the contact pair must be balanced by the resultant load from the hydrodynamic pressure in the lubricant film L, which is obtained by integration of the pressure over the contact. This is achieved by finding the proper distance between the solid bodies. In this work, the approach of Hajishafiee et al. [54,59] is followed. It expresses the rigid displacement update (increment) per load balance iteration as:

$$\Delta h_d = (|v|_{max} - |v|_{min}) \frac{L_{ext} - L}{L_{ext}} \frac{\Delta t}{t_d} r_d \tag{36}$$

where $t_d = {}^{R}/_{a_s}$ is a characteristic deformation time, a_s is the sonic velocity in the solid material, r_d is an under-relaxation factor, $|v|_{max}$ and $|v|_{min}$ are the maximum and minimum deflection in the solid domain, respectively. Moreover, the ratio $\frac{\Delta h_d}{\Delta t}$ is limited by the prescribed maximum solid body velocity of 0.002 m/s.

3. Numerical procedure

The HEM model and lubricant properties libraries have been implemented in OpenFOAM. For the fluid-solid interaction problems, the solids4Foam toolbox of Cardiff et al. [68] has been employed to couple the fluid and solid domains. The governing equations described in the previous section were discretized by the Finite Volume Method (FVM). A pseudo-transient code is used to obtain the steady-state solution. The time increment is chosen in the order of nanoseconds. To ensure that the solution has reached steady-state condition, the numerical solution for pressure, temperature, solid displacement, and central film thickness should converge to a final, accurate result with a relative tolerance of 10^{-6}. In addition to steady-state conditions for fluid and solid variables, the load should converge to the target load with an error of 0.1%.

The authors emphasize that in the simulations throughout this work, the wave asperities remain stationary and are not physically moved. The asperity movement is instead simulated by imposing a constant velocity vector on the no-slip boundaries, as if a snapshot was taken from the contact. The reason for adopting a pseudo-transient simulation strategy is motivated by the current limitations of the fully transient OpenFOAM TEHL model to include both elastic deformation of the surface and the asperities by means of FSI, and the superimposed rigid body motion of the rotating geometry simulating the translational movement of the deformed asperities in the contact. This development is part of future research and is not yet available at this moment. However, we believe that the current pseudo-transient approach already gives useful insight and that the adopted level of CFD-FSI modelling has the advantage of providing a better understanding of the tangential deformation of the asperities, the temperature effect in wavy contacts and a more detailed view of the (sub-surface) stresses in the solid material.

The focus of the current study is on illustrating the difference in using an equivalent or two-body geometry for rough TEHL. We believe that the current pseudo-transient method is sufficient for this purpose, but we also expect quantitative differences with a full transient approach due to transient effects that are neglected. Besides the comparison between both geometrical methodologies, this work represents a first step toward the comprehensive transient modelling of deterministic rough contacts. This level of TEHL numerical modelling allows for enhancing comprehension, at least for particular solutions of rough TEHL contacts.

A schematic view of the 2D computational grid is shown in Figure 2. According to a mesh independency study, a computational grid with 10000 cells in the fluid domain and 22000 cells for each solid region has been used.

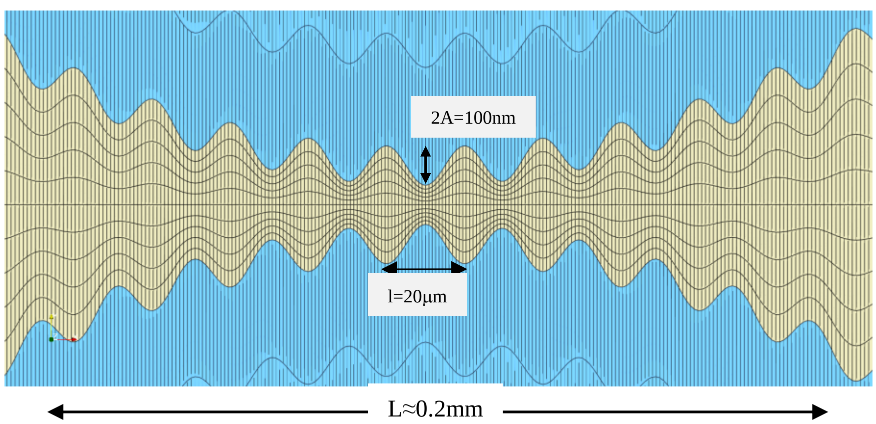

Figure 2 Computational grid at the contact.

A partitioned approach has been applied to couple the fluid and solid solvers, in which the interface displacement is determined using an Aitken or filtered IQN-ILS algorithm [69,70]. Between 4 to 8 iterations are required to reach convergence up to 10^{-8} in each time step. As a result, the conditions described in equations (33) and (34) are fully satisfied. A schematic of the coupling approach is illustrated in Figure 3.

Figure 3 FSI coupling algorithm.

FSI algorithm

Start FSI for the new time step

Update load balance and rigid displacement

Do

Calculate the relaxation factor for the coupling algorithm
Adjust displacement based on the coupling algorithm
Move the fluid mesh
Solve fluid equations
Transfer the forces acting on the interface from fluid to solid
Solve structural equations

While (FSI loop not converged)

4. Validation

The developed CFD-FSI solver for TEHL is evaluated for different cases with different operating conditions. As experimental measurements of TEHL line contacts using the same lubricant are not available, we follow the common approach used in literature to validate the current CFD-FSI model against well-documented computational data from three different independent sources in literature, i.e. Hartinger et al. [52,58], Tosic et al. [71,72] and Srirattayawong [73]. Fluid properties and operating conditions for the cases mentioned above have been obtained from the corresponding references to make an accurate comparison. Note that with the exception of Hartinger, all validation cases are isothermal.

Figure 4 clearly illustrates that the developed CFD-FSI solver's results show excellent correspondence with the CFD-Boussinesq solution presented by Tosic et al. [74] and Hartinger et al. [52]. The five validation configurations of the two cases studied here consist of pure rolling, pure sliding, isothermal, non-isothermal, and target loads of $100\ \mathrm{kN/m}$ and $50\ \mathrm{kN/m}$. It is clear from the results that the developed TEHL model in OpenFOAM properly represents the involved physics in comparison with comparable data from the literature and provides reliable and trustworthy results.

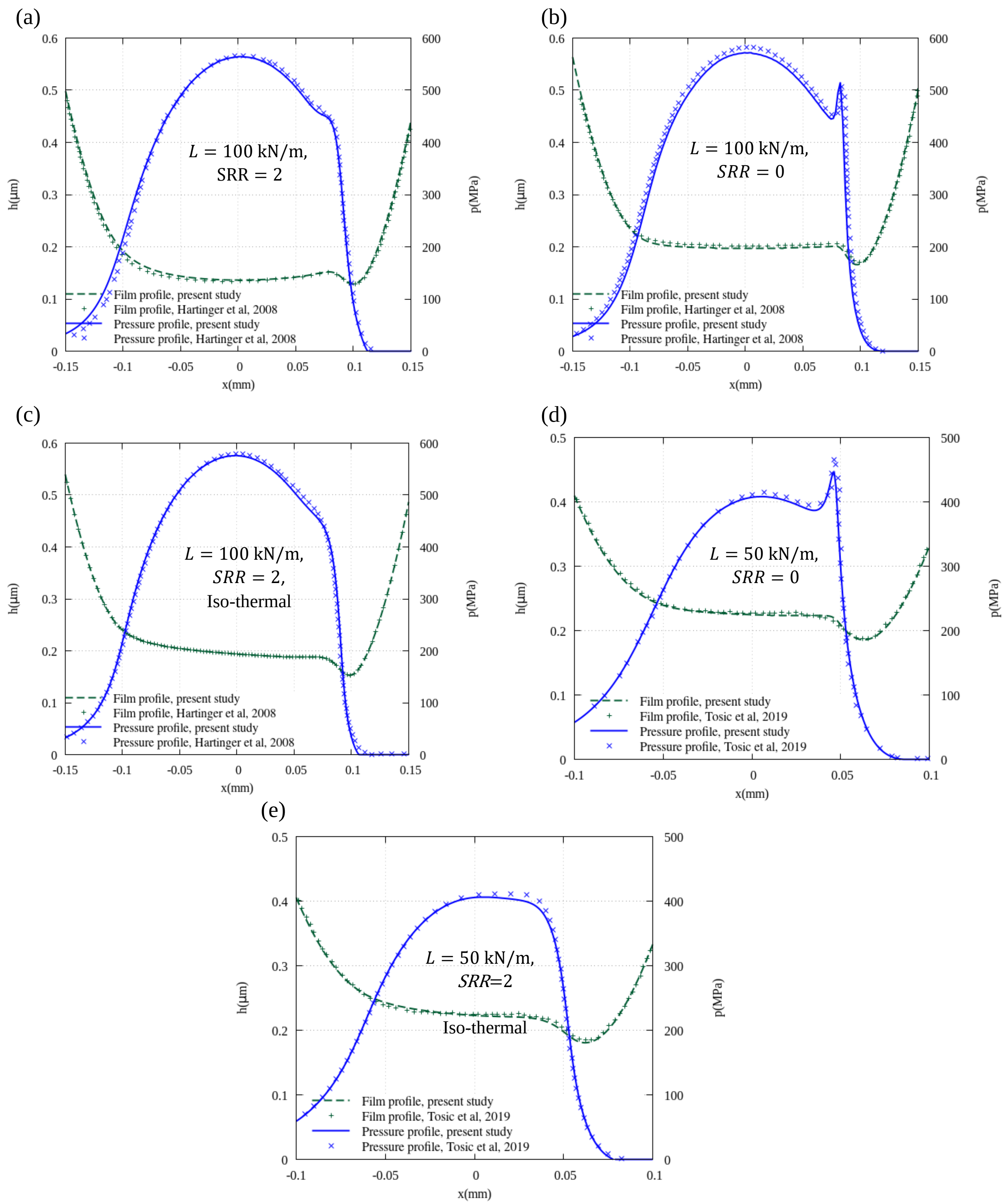

Figure 4 Validation of numerical results, for $L = 100\ kN/m$, $E_r = 345$ GPa; a) $SRR = 2$ and non-isothermal. Isothermal solution for b) $SRR = 0$ or pure rolling, c) $SRR = 2$ or pure sliding. Another test case for $L = 50\ kN/m$, $E_r = 362.5$ GPa and isothermal solution of d) $SRR = 0$, e) $SRR = 2$.

5. Results

Squalane is selected as the lubricant of interest in this work since its thermomechanical properties are well documented in the literature, e.g. by Bair [62,75], and the parameters in the EoS and viscosity model can be set regarding numerical studies which used the same lubricant [18,76]. All lubricant and solid parameters are listed in Table 3.

Table 3 Lubricant and solid parameters for constitutive models

	Parameter	Value	Dimension
Equation of State [75]	Liquid density at ambient pressure	$\rho_R = 794.6$	$\mathrm{kg/m^3}$
	Vapour density at saturation pressure	$\rho_{v,sat} = 0.0288$	$\mathrm{kg/m^3}$
	Saturation pressure	$p_{sat} = 5000$	Pa
	Rate change of isothermal bulk modulus at zero pressure	$\acute{K}_0 = 11.74$	-
	Thermal expansion defined in the volume ratio	$a_V = 8.36 \times 10^{-4}$	$\mathrm{K^{-1}}$
	K_0 at zero absolute temperature	$K_{00} = 8.658$	GPa
	Temperature coefficient of K_0	$\beta_k = 6.332 \times 10^{-3}$	$\mathrm{K^{-1}}$
	Inlet temperature	$T_0 = 313.15$	K
	Reference temperature	$T_R = 313.15$	K
Viscosity [75]	Dynamic viscosity of vapor	$\mu_v = 8.97 \times 10^{-6}$	Pa s
	Dynamic viscosity of liquid at ambient condition	$\mu_R = 0.0157$	Pa s
	Doolittle parameter	$B = 4.71$	-
	Occupied volume fraction at reference state, $T_R, p = 0$	$R_0 = 0.6568$	-
	Occupied volume thermal expansivity	$\varepsilon = -7.273 \times 10^{-4}$	$\mathrm{K^{-1}}$
	Liquid critical shear stress or shear modulus of lubricant	$G_{c,0} = 6.94$	MPa
	Power law exponent	$n = 0.463$	-
	Limiting stress pressure coefficient	$\Lambda = 0.075$	-
Thermal [75]	Parameter in the heat capacity function	$m = 0.62 \times 10^6$	$\mathrm{J/m^3\ K}$
	Parameter in the heat capacity function	$C_0 = 0.94 \times 10^6$	$\mathrm{J/m^3\ K}$
	Coefficient in the conductivity equation	$A = -0.115$	-
	Parameter in the conductivity function	$C_k = 0.074$	W/mK
	Exponent in the conductivity model	$s = 4.5$	-
	Coefficient in the conductivity equation	$q = 2$	-
Solid [54]	Elasticity Modulus	$E = 200$	GPa
	Poisson Ratio	$\vartheta = 0.3$	-
	Density	$\rho_s = 8750$	$\mathrm{kg/m^3}$
	Equivalent curvature	$R_e = 10$	mm
	Specific heat capacity	$C_s = 450$	J/kg K
	Thermal conductivity	$k_s = 47$	W/mK

In the following, the effects of surface waviness on TEHL line contacts between two rolling bodies with identical but opposite radii of curvature are investigated. Two commonly used and seemingly interchangeable contact conjunction geometries are considered, i.e.

1. The reduced equivalent geometry of an equivalent roller against a rigid flat plate, as traditionally used in EHL studies, relying on Hertzian-Boussinesq theory, and
2. The real contact conjunction formed by two roller bodies

In current work, the waviness which is superimposed on both bodies is limited to a sinusoidal surface profile, with the form:

$$\acute{h}_i(x) = A_i \sin\left(\frac{2\pi}{l_i}x + \varphi_i\right) \tag{37}$$

If the equivalent geometry is used, then the following equivalent surface profile should be used (for $A_1=A_2=A$ and $l_1=l_2=l$):

$$\acute{h}_e(x) = 2A\, sin\, \left(\frac{2\pi}{l}x\right) cos\frac{\Delta\varphi}{2} \tag{38}$$

Parameters A, l, φ denote the wave amplitude, wavelength, and phase (i.e., the relative position to the origin), respectively. In the following, the effect of those three parameters on the pressure and temperature distribution, as well as the film thickness and the coefficient of friction (CoF), will be investigated in detail. Thereto, we consider a TEHL case where two oil-lubricated parallel-axis cylindrical rollers ($E = 200$ GPa, $\vartheta = 0.3$), each with a radius of 20 mm, are rolling with slip, under a normal external load of 100kN/m. Considering the reduced geometry, the equivalent reduced radius of curvature is found to be 10mm. According to Boussinesq-Hertz theory, the equivalent elasticity modulus would be $E_r = \frac{\pi E}{2(1-\vartheta)} \approx 345$ GPa. Because a linear elastic solver is used, the equivalent cylindrical roller body has an equivalent modulus of $E_{eq} = E/2 = 100$ GPa with a Poisson ratio $\vartheta = 0.3$), whereas the solid plate is considered rigid ($E = \infty$). The SRR is varied between $0 - 2$, and an entrainment velocity of 2.5 m/s is considered in this study. For instance, with $SRR = 1$, the cylinders rotate at 596 rpm and 1790 rpm, which corresponds to the aforementioned entrainment velocity. Surface topographies listed in Table 4 are investigated. Note that the topography amplitude A is significant in comparison with the film thickness, which has a minimum value in the order of ± 200 nm.

It is noteworthy that to calculate the CoF, one must consider the summation of forces acting on either the upper or lower surface in the flow or tangential direction. Hence, the CoF reported in this study has been calculated according to the following formula:

$$CoF = \frac{F_\tau + F_t}{F_n} = \frac{\int \overrightarrow{\tau_w}.\overrightarrow{e_t}dA + \int p.\overrightarrow{e_t}dA}{\int p.\overrightarrow{e_n}dA} \tag{39}$$

where $\overrightarrow{\tau_w}$ is the shear forces and $\overrightarrow{e_t}$ indicates the tangential unit vector of the surfaces. Also, the SRR is defined as:

$$SRR = \frac{u_1 - u_2}{\frac{u_1 + u_2}{2}} \tag{40}$$

where subscripts 1 and 2 denote upper and lower surfaces, respectively.

The thermal conductivity of the solids in the present work is set at $k_s = 47$ W/mK, which has been taken from similar studies [18,53,54,77] for steel in annealed condition. For hardened steel, the thermal conductivity is significantly lower. The sensitivity of the final solution and variation of contact variables to the solid's thermal conductivity have been investigated. In brief, a similar trend and conclusion have been obtained, whereas it has little influence on the temperature, pressure, and film thickness. With a thermal conductivity of $k_s = 19$ W/mK, a little thinner film, a few degrees higher temperature, lower pressure ripples, and around 10% lower CoF are calculated. These findings are also in agreement with Habchi and Bair's work on the influence of hardening on TEHL solutions [78]. Hence, we are confident that the qualitative trends and conclusions obtained in this work are not sensitive to the precise value of the thermal conductivity.

Table 4: Overview of simulated cases for both equivalent and two-body geometries.

Goal	Name	A_1/A_2 [nm]	l_1/l_2 [µm]	φ_1/φ_2 [rad]
Reference case	Case 1	50/50	20/20	$\frac{\pi}{2}/\frac{\pi}{2}$
Amplitude variation	Case 2	25/25	20/20	$\frac{\pi}{2}/\frac{\pi}{2}$
	Case 3	50/25	20/20	$\frac{\pi}{2}/\frac{\pi}{2}$
	Case 4	50/75	20/20	$\frac{\pi}{2}/\frac{\pi}{2}$
Wavelength variation	Case 5	50/50	10/20	$\frac{\pi}{2}/\frac{\pi}{2}$
	Case 6	50/50	40/20	$\frac{\pi}{2}/\frac{\pi}{2}$
Phase shift	Case 7	50/50	20/20	$\frac{\pi}{2}/\frac{3\pi}{4}$
	Case 8	50/50	20/20	$\frac{\pi}{2}/\pi$
	Case 9	50/50	20/20	$\frac{\pi}{2}/\frac{5\pi}{4}$
	Case 10	50/50	20/20	$\frac{\pi}{2}/\frac{3\pi}{2}$

Firstly, the effects of waviness amplitude in equivalent geometry will be investigated for $A = 25 - 125$ nm and $l = 20$ µm. Secondly, a fixed sinusoidal surface profile with parameters $l_1 = 20$ µm, $A_1 = 50$ nm, and $\varphi_1 = \frac{\pi}{2}$ is imposed on the elastic upper surface, whereas a similar sinusoidal surface profile is imposed on the countersurface for which the influence of amplitude A_2, wavelength l_2 and phase shift φ_2 is investigated. We emphasize once more that steady-state simulations have been performed, ignoring opposing surface waves' explicit motion. Therefore, the simulation results should be interpreted as snapshots of non-smooth surface motion and provide useful details of contact at discrete steps as such. The validity of this assumption is presented in Appendix C.

5.1. Comparison equivalent vs two-body approach

A comparison has been made to highlight the difference between the two approaches explained above. In this case study, the total amplitude is 100 nm, and the wavelength is 20 µm; also, there is no phase difference (case 1).

Figure 5 shows the film thickness, pressure, heat flux, and shear stress at the interface for the two explained approaches. Corresponding to the film thickness reduction and fluctuation in pressure, a monotonous increase of the maximum of the normal and tangential stresses are observed, accompanied by an increase of the maximum temperature in the contact. Moreover, the shear stress at the surfaces fluctuates in contact; it is influenced by piezo-viscous effects and the fluid velocity gradient. Figure 6 presents the variation of average viscosity on the contact region and shows the shear-thinning and thermal effects on the calculated viscosity. Note that the average has been taken over both flow and across film directions. Piezoviscous effects are reduced by about 85% as a result of thermal effects, and by 70% due to shear-thinning effects, indicating the importance of including thermal and non-Newtonian effects in the TEHL contacts modelling.

It is evident that maximum pressure, shear stress, and heat flux are significantly higher when the surface profiles are imposed on the equivalent deformable body. The main reason behind this is related to the traction forces on the deformable bodies. Figure 7-a presents the deformation of the solid bodies along the flow direction. It clearly indicates that the shear stresses at surfaces lead to moving asperities on the upper body to the right and the lower body to the left. The surface features first met each other at the center of contact and completely overlapped each other (without phase difference), whereas a phase difference is introduced due to elastic deformation when the contact is under an external load. The wave crests were moved by $\approx 5\ \mu\text{m}$ in this case study, which is approximately equal to $1/4$ of the wavelength; in other words, the phase difference is $\approx \frac{\pi}{2}$. Also, Figure 7-a reveals that the asperities' deformation in the tangential direction is greater in the two-body geometry than in the equivalent geometry. Note that despite the fact that the equivalent body also undergoes a tangential deformation, it cannot incorporate the effects of relative movement of asperities. The tangential displacement in the outlet region is due to the tangential forces on the macro-scale, whereas tangential displacement occurs at the inlet region due to pressure fields and shear stress that are taken up by elastic displacement.

Figure 7-c and Figure 7-d show the temperature field in the contact. Underneath each surface peak, one clearly observes a significant local temperature rise, which obviously depends on the shear rate and viscosity. This local increase in temperature is caused by higher viscous shear heating due to higher shear rates in the gap underneath each peak. Due to higher shear heating, the temperature increases locally, followed by a drop in viscosity. The maximum fluid temperature in the equivalent case is 362 K, while it is 354 K in the two-body case with a total amplitude of 100 nm. Indeed, the temperature oscillation in the contact is amplified as the amplitude of surface waviness increases. Note that viscous heating underneath each peak is dominant. A similar temperature variation has been observed in [59], which employed the CFD-FSI technique for the TEHL simulation of a different case.

Comparing the results of the equivalent and two-body geometries indicates that the overall trend of temperature variations is similar. However, the maximum temperature rise in the contact is 8 K (19.4%) lower for the two-body geometry. Due to elastic deformation, the velocity profile and its gradient are influenced; therefore, the shear heating at the contact can be different, leading to deviation in the temperature field. Also, the Carslaw-Jaeger boundary condition considers one-dimensional heat transfer, while heat can be transported in both normal and tangential directions in solid materials.

Figure 8 shows the deviations in contact variables predicted by the equivalent geometry and two-body geometry. The central film thickness is about 20% thicker in the case of two-body, whereas the maximum pressure and von Mises stress are 17% and 30% lower, respectively. On the other hand, the CoF is only influenced by 24%, while the maximum shear stress is changed by 42%. In conclusion, this case study shows the potential deviation in using equivalent geometry in combination with Carslaw-Jaeger boundary conditions for the rigid plate in comparison with the two-body approach, where both surface waviness is modelled explicitly.

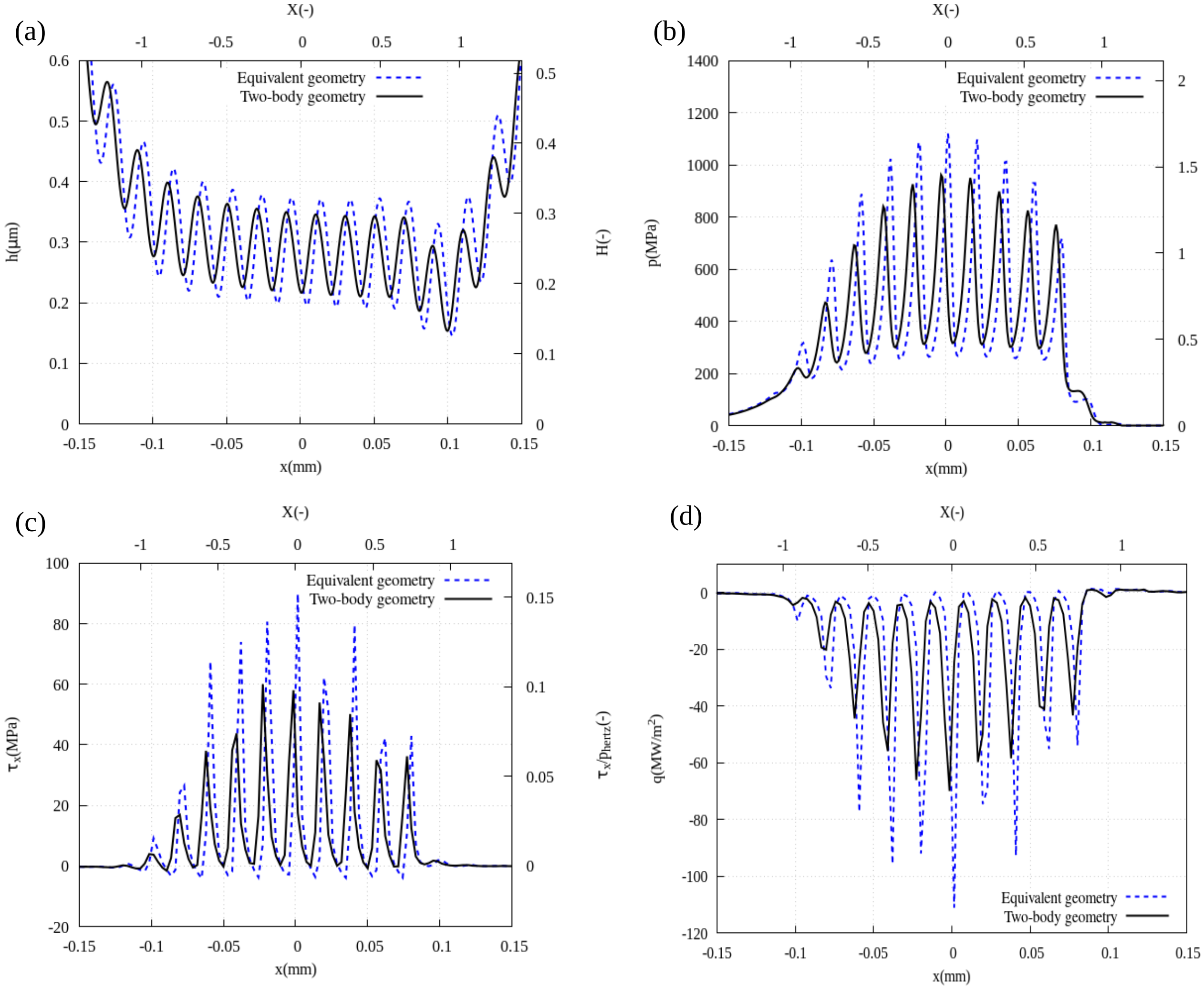

Figure 5 Comparison of equivalent geometry with superimposed surface profile and two-body geometry. a) film thickness, b) pressure, c) shear stress, and d) heat flux profiles. The total amplitude is 100nm. The operating condition is $L = \frac{100\text{ kN}}{\text{m}}, E_r = 345\text{ GPa}, SRR = 1$.

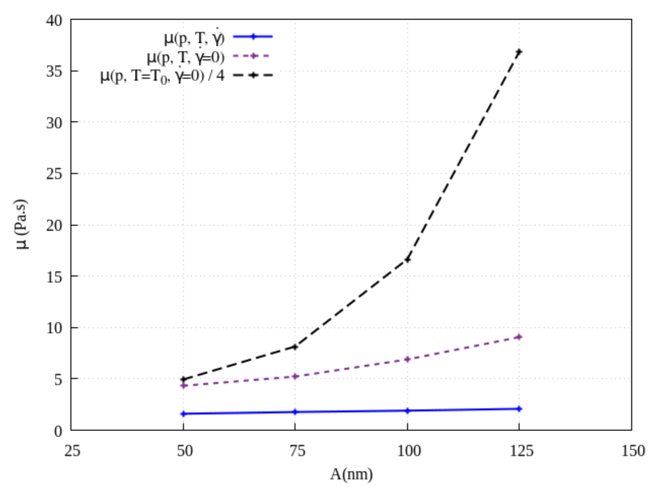

Figure 6 Variation of average viscosity (on the contact region) with amplitude of surface waviness for two-body cases. The operating condition is $L = \frac{100\text{kN}}{\text{m}}, E_r = 345\text{GPa}, SRR = 1.$

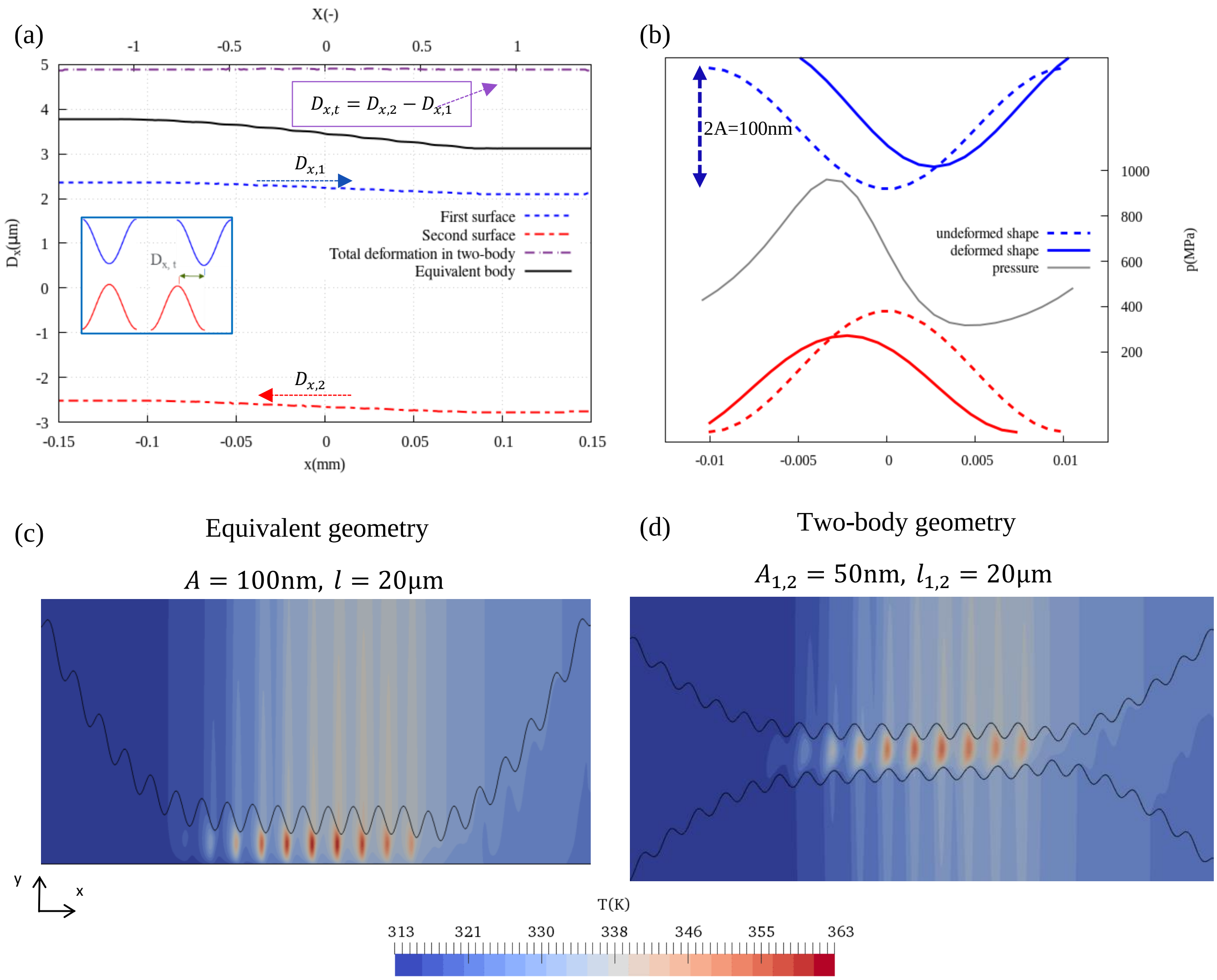

Figure 7 Comparison of equivalent and two-body approaches. a) tangential displacement of surfaces, b) the undeformed and deformed shape of a single asperity along with the pressure acting on it (dashed lines show undeformed and solid lines show the deformed asperity), c) temperature profile of the equivalent case, and d) temperature profile of the two-body case. The total amplitude is 100nm. The operating condition is $L = \frac{100\text{ kN}}{\text{m}}, E_r = 345\text{ GPa}, SRR = 1.$

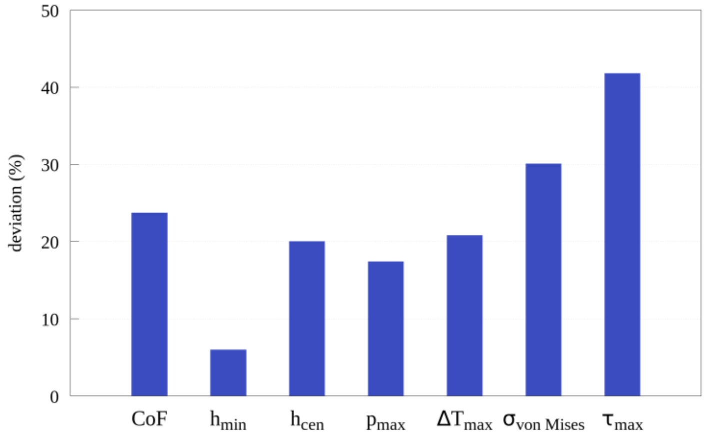

Figure 8 Deviation in contact variables predicted by equivalent geometry and two-body geometry. The operating condition is $L = \frac{100\ \mathrm{kN}}{\mathrm{m}}, E_r = 345\ \mathrm{GPa}, SRR = 1$.

A more detailed evaluation of equivalent and two-body approaches for smooth and waviness profiles has been conducted for solid stresses. In TEHL contacts, the stress levels in the solid materials largely determine the lifetime of the mechanical components for a given material and load spectrum. Figure 9 shows the von Mises stress in the solid material for a smooth and a rough contact with $A = 50\ \mathrm{nm}, l = 20\ \mu\mathrm{m}$ for the equivalent geometry and $A_1 = A_2 = 25\ \mathrm{nm}, l_1 = l_2 = 20\ \mu\mathrm{m}$ for the two-body geometry. It can be observed that both maximum von Mises stress and its location are changed in the rough case. The maximum equivalent stress is 310 MPa, 345MPa and 422 MPa for the smooth, rough equivalent contacts and real rough contacts with two bodies, respectively. It is worth noting that the location of maximum stress in the smooth contact is $\frac{y}{a} = 0.78$, which is in agreement with the traditional theory based on the Hertzian contact, while it is located at the surface in the rough case, as also observed in [79]. This difference is because the local shear stress increases significantly in the rough contacts; hence, maximum von Mises stress has moved from the sub-surface to the surface. This indicates a potentially higher chance of surface fatigue than sub-surface fatigue. This is out of scope in the current study and requires further investigations in future work.

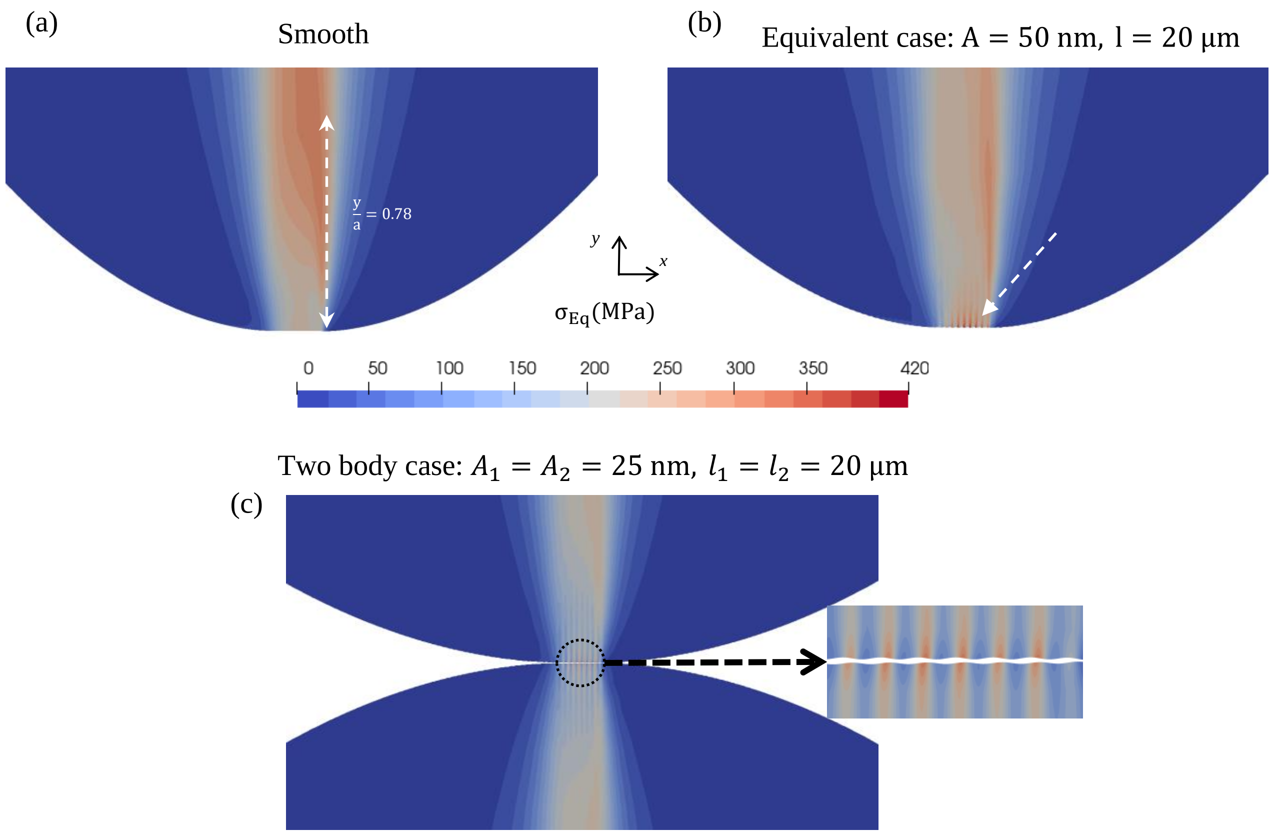

Figure 9 Von Mises stress in solid material for a) a smooth and b) rough contact with the equivalent geometry and equivalent waviness with a total amplitude of 50 nm and wavelength of 20µm, c) rough contact with two-body geometry. Each surface has a wavy profile with an amplitude of 25 nm and wavelength of 20 µm.

Worthwhile to mention is also the solid stiffness of individual asperities in both studied approaches. The stiffness for a single asperity is defined as an integration of pressure over a wavelength divided by average deformation in the normal direction. We observed that a single asperity carries an almost equal load in the equivalent and two-body methods. However, because of the different modulus of elasticity, the total deformation of the asperities differs in both approaches, resulting in different stiffness coefficients. In brief, for the case of $\mathrm{A} = 100$ nm, $\mathrm{l} = 20$ µm, the load of ≈ 11 kN/m is carried by a single asperity in the center of contact, whereas the stiffness of equivalent asperity is $k_{Eq} = 2.42$ (GN/m)/m and $k_1 \approx k_2 \approx 3.05$ (GN/m)/m. It should be underlined that although an equal stiffness was expected based on the half-space assumption for Hertzian contact, this does not hold for a single asperity analysis.

5.2. Influence of the amplitude ($l_2 = 20$ µm, $\varphi_2 = \frac{\pi}{2}$, $SRR = 1$)

In this section, the effects of the amplitude of surface waviness on the lubrication condition of TEHL contact are investigated. In addition, the deviations between using equivalent geometry and two-body geometry are also illustrated for different amplitudes (cases 1-4).

For a maximum wave amplitude of $A_2 = 75$ nm, the minimum and central film thickness are reduced by 38% and 27% in comparison with the smooth contact, respectively. In contrast to the tendency of the minimum film thickness, the average lubricant film thickness slightly increases with the increasing amplitude of the second surface waviness, as shown in Figure 10-c. Indeed, for the double-sided waviness with $A_2 = 75$ nm, an increase of 3.6% in average film thickness in comparison with the smooth surface. The average film thickness has also been increased in [8], which used the iso-thermal solution of the Reynolds-Boussinesq approach in different operating conditions.

As expected, the hydrodynamic pressure profile displays a local maximum near each surface peak; however, the pressure spikes are not sinusoidal due to the nonlinear dependency of pressure on film thickness, and the nonlinear constitutive behaviour of the lubricant. A higher peak in the surface profile leads to a higher pressure fluctuation in the contact. From Figure 10-c and Figure 10-d, one can clearly observe that the maximum peak pressure increases almost linearly with increasing amplitude A_2, reaching approximately 1.63 and 1.76 times the maximum Hertzian pressure in the case of $A_2 = 50$ nm and 75 nm. The von Mises stress can increase up to 67% in the two-body case, with $A_2 = 75$nm in comparison with a smooth case, as shown in Figure 10-d. Also, the maximum shear stress increases considerably to 77 MPa in the two-body case, whereas the CoF is slightly changed. Also, the maximum von Mises stress is about $45\% - 50\%$ of the maximum lubricant pressure. Local pressure and shear stress determine the maximum von Mises stress, which are nonlinearly influenced by global and local geometry, film thickness, load, and velocity. Because the surface profile also affects the local geometry, clearance, and shear stress, the ratio between von Mises stress and lubricant pressure is slightly different due to nonlinearity for studied waviness profiles.

Further, a monotonous increase of the temperature rise within the contact is observed with an increasing wave amplitude of the second surface waviness, which counteracts the piezo-viscous effect in the high pressure region.

Figure 10 shows contact variables for both the equivalent and two-body approaches explained above. Deviations between $5\% - 26\%$ in CoF and $3\% - 13\%$ in minimum film thickness are observed between both approaches. About a $3\% - 21\%$ difference is observed in maximum contact temperature rise and $7\% - 17\%$ in maximum pressure, whereas the difference in maximum von Mises stress increases between $20\% - 30\%$. The pressure and stresses are overestimated in the equivalent case due to a lack of elastic deformation of asperities in comparison with the two-body method, affecting the viscosity and temperature field. Furthermore, the film thickness is underestimated due to the higher temperature at the contact.

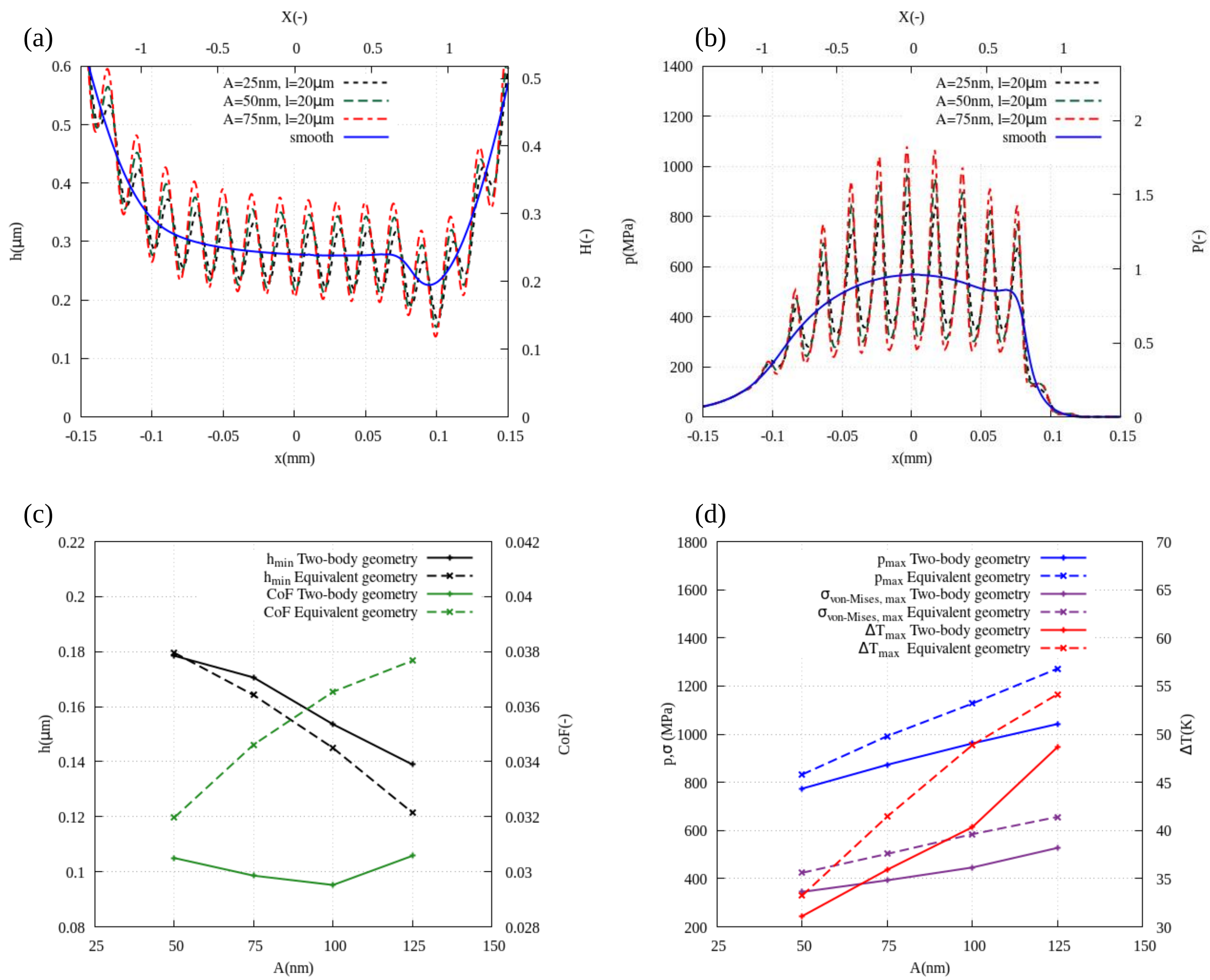

Figure 10 Effect of the amplitude of surface asperities imposed on the second surface on a) lubricant film thickness, b) pressure, c) minimum film thickness and CoF, d) maximum pressure, von Mises stress, and temperature rise. $L = \frac{100\text{ kN}}{\text{m}}, E_r = 345\text{ GPa}, SRR = 1, l_1 = l_2 = 20\text{ μm}, A_1 = 50\text{ nm}$, and $\varphi_{roller} = \frac{\pi}{2}$.

5.3. Influence of wavelength $\left(A_2 = 50\text{ nm},\ \varphi_2 = \frac{\pi}{2},\ SRR = 1\right)$

Let us consider the effect of wavelength difference between both surface waviness, with equal amplitudes and zero-phase shift (case 1 and case 5-6). We emphasize that due to the difference in wavelength between both surfaces' waviness, the resulting film thickness always contains two superimposed sinuses with different wavelengths, potentially leading to a variable amplitude film thickness. This implies that the pressure and temperature responses between different cases might change more drastically than in previous comparisons so far.

Figure 11 shows the film thickness and the pressure profiles, as well as the maximum pressure and temperature values and the coefficient of friction for the variable wavelength of the lower surface profile, i.e. l_2 in the range $10\text{ μm} - 40\text{ μm}$. In Figure 11-a, we observe that the increase in the wavelength of the lower surface results in a dual-mode film profile with increasing maximum amplitude. Note that for $l_2 = 40\text{ μm}$, amplitude modulation is witnessed, which is also reflected in the corresponding pressure profile. Due to the amplitude increase, a monotonous increase of minimum film thickness with the increasing wavelength of the second surface is observed in Figure 11-c. Though more pronounced, it closely resembles the witnessed behaviour for variable amplitude. The minimum film thickness increases by about 6% as the wavelength of the lower surface profile increases from 10 μm to 40 μm. The average film thickness remains stable.

Although the pressure profiles clearly reflect the film thickness profile, interpretation of the tendencies for maximum pressure and temperature values in Figure 11-d is not straightforward because each situation is different due to the superposition of two wavelengths. For the cases simulated in this work, however, we observe an increase of the CoF with increasing wavelength.

While a monotonous increase has been observed for maximum pressure, temperature, and von Mises stress, these values show a very small reduction when the wavelength increase from 10μm to 20 μm. The difference in temperature rise and maximum pressure predicted by equivalent and two-body approaches vary between $2\% - 27\%$ and $6\% - 23\%$, respectively. Also, the CoF is predicted to be about 20% higher in equivalent geometry with a superimposed surface profile, whereas the minimum film thickness is $6\% - 13\%$ lower in this approach.

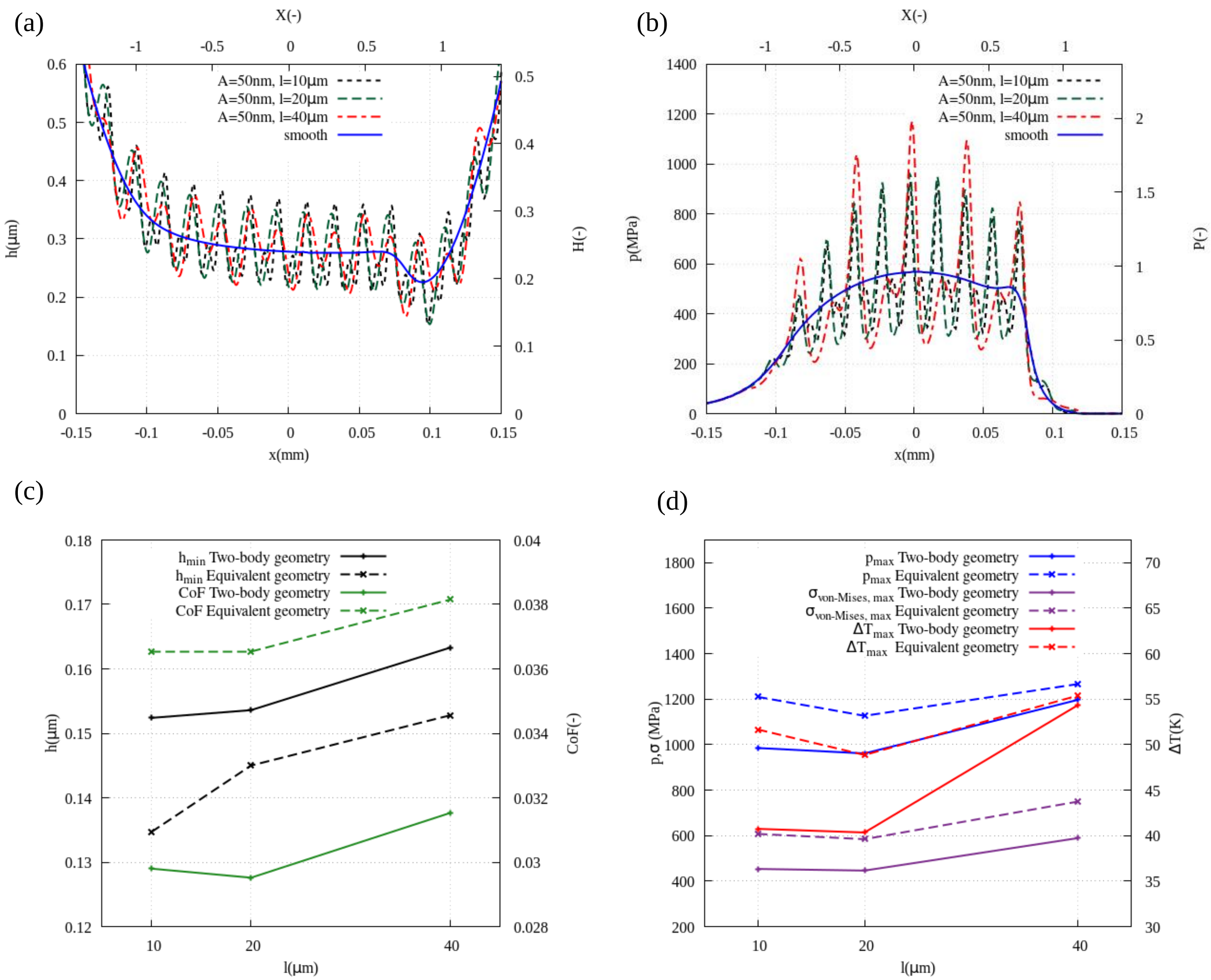

Figure 11 Effect of the length of surface asperities imposed on the second surface on a) film thickness, b) pressure, c) minimum film thickness and CoF, d) maximum pressure, von Mises stress, and temperature rise. $L = \frac{100\ \mathrm{kN}}{\mathrm{m}}, E_r = 345\ \mathrm{GPa}, SRR = 1, l_1 = 20\ \mathrm{\mu m}, A_1 = A_2 = 50\ \mathrm{nm}$, and $\varphi_1 = \frac{\pi}{2}$.

5.4. SRR effects

The effects of the waviness of surfaces in TEHL conditions are investigated in pure rolling and pure sliding conditions, where dominant terms are different. Figure 12 shows film thickness, pressure, and contact variables as a function of SRR. In pure rolling conditions (SRR=0), temperature changes are limited to a few degrees of Celsius, and viscosity is varied only due to piezoviscous effects. Hence, the pressure is higher; subsequently, viscosity is higher for pure rolling conditions in comparison with SRR>0, and a thicker film is established. The two-body approach predicts a thicker film along with a considerably lower pressure at the contact in pure rolling conditions. The maximum pressure and maximum von Mises stress are 27% and 23% higher in equivalent geometry, respectively. Furthermore, the local maximum shear stress is significantly higher at rolling conditions; it has been 57% overestimated in the equivalent geometry.

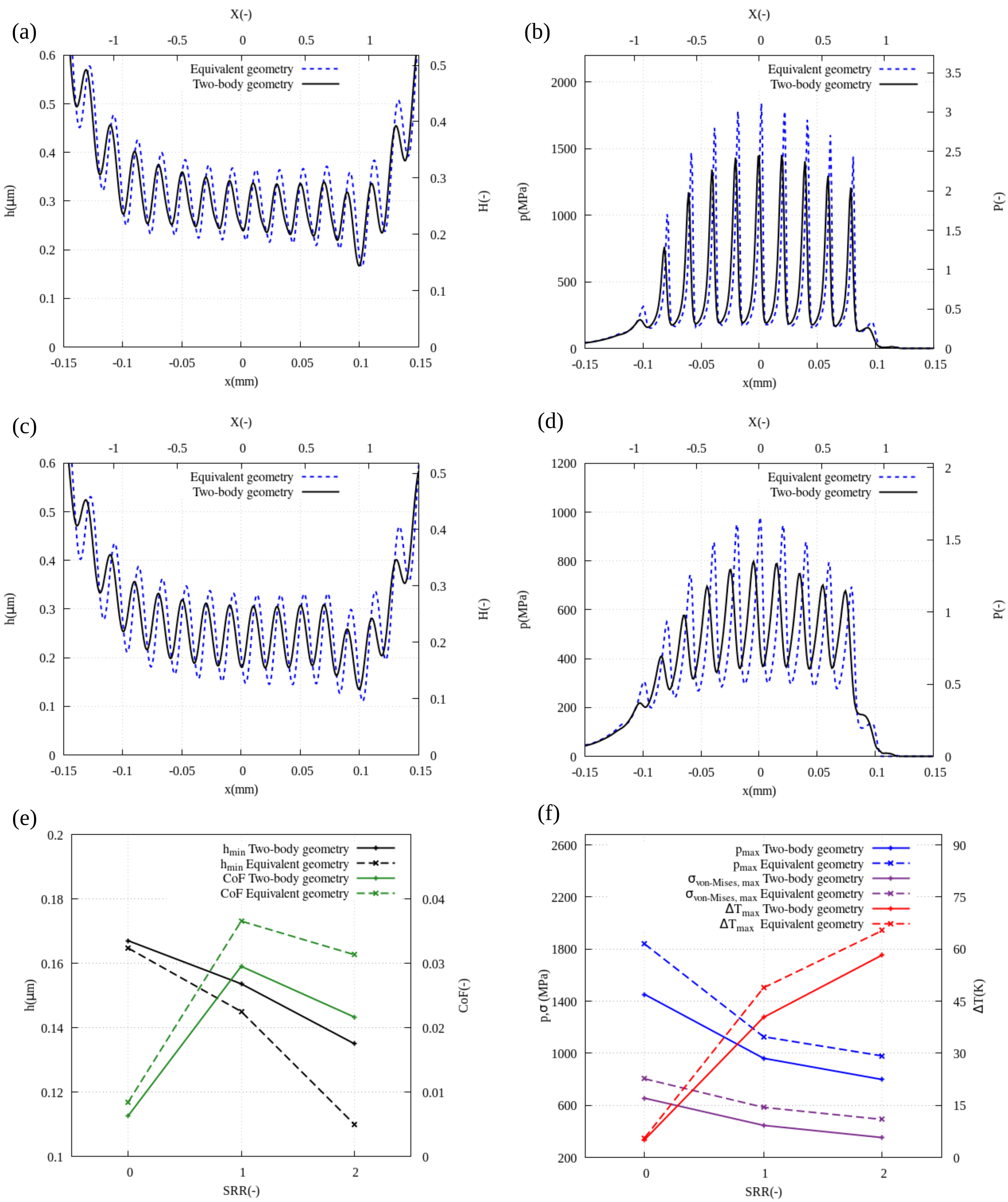

Figure 12 a) lubricant film thickness and b) pressure profile for pure rolling condition, c) and d) same profiles for pure sliding condition, e) minimum film thickness and CoF, f) maximum pressure, von Mises stress, and temperature rise. $L = \frac{100\ \text{kN}}{\text{m}}, E_r = 345\ \text{GPa}, l_1 = l_2 = 20\ \mu\text{m}, A_1 = A_2 = 50\ \text{nm}, \text{and}\ \varphi_{roller} = \frac{\pi}{2}$.

For pure rolling conditions, the CoF is much lower in the case of smooth surfaces in comparison with wavy surfaces. The CoF consists of two components: the viscosity induced shear forces and the pressure-induced tangential force. For pure rolling in wavy contacts, the shear stress contribution is low in comparison with the tangential forces associated with the pressure field. For pure sliding conditions, the higher shear rate results in higher viscous heating and hence contact temperature, leading to a decrease in viscosity and CoF. Moreover, a thicker film and lower pressure are observed in the two-body geometry. The difference between both approaches is about 23% for the maximum pressure and 39% for the maximum von Mises stress. Furthermore, the CoF, the maximum temperature, and the minimum film thickness were overestimated by respectively 45%, 12%, and 18% for SRR=2. In conclusion, in comparison with the two-body approach, using an equivalent body results in an underestimation of film thickness and an overestimation of the pressure, temperature, and CoF for three different studied SRRs of 0, 1, and 2.

In contrast to a full transient simulation, the current approach does not allow to observe of the double wavelength in film thickness and pressure profiles under sliding conditions. Indeed, the transient inlet modulation of film and pressure might stimulate pressure rise in sliding conditions [80], which are not taken into account here.

5.5. Phase-shift effect ($A_2 = 50$ nm, $l_2 = 20$ µm, $SRR = 1$)

Finally, we investigate the effect of phase-shift between similar sinusoidal profiles, i.e. with equal amplitude and wavelength, on both surfaces (cases 7-10). The phase of the second surface (lower body) waviness is varied from $\varphi_2 = \frac{\pi}{2}$ to $\varphi_2 = \frac{3\pi}{2}$, covering half a period, whereas $\varphi_1 = \frac{\pi}{2}$. This implies that opposing peaks are in phase, i.e. $\Delta\varphi = 0$, in counter phase, i.e. $\Delta\varphi = \pi$ or in between, simulating surface peaks at different relative positions. We emphasize once more that although the asperities are constantly in relative motion to each other in reality, we consider here steady-state calculations, representing instantaneous snapshots in time.

Figure 13 displays the results for the film thickness, surface deformation in the streamwise direction, pressure and temperature profile for various phase shifts. The results of the smooth case are depicted as a reference.

For aligned sinusoidal surface profiles ($\Delta\varphi = 0$), one clearly observes that the amplitudes of the fluctuations in both the film thickness and pressure profiles are maximal. By increasing the phase shift $\Delta\varphi$, these amplitudes are reduced until a minimum is reached near $\Delta\varphi = \frac{\pi}{2}$, resulting in a smoother film thickness and corresponding pressure profile. Furthermore, the amplitude increases for textures that are in counter-phase ($\Delta\varphi = \pi$), which is not expected in advance. Note that the equivalent roller has a smooth profile for $\Delta\varphi = \pi$, which is obviously not correct. The described trend is clearly visible when looking at the contact variables in Figure 14. The central and minimum film thickness vary by 28% and 24% in a single period. Moreover, the pressure abruptly increases over this period from 1.1 to 1.63 times the maximum Hertzian pressure. Similar results were also observed by Almqvist and Larsson [1] for a ridge-ridge overtaking event.

Looking at the streamwise component of the solid deformation vector at the surface, one clearly observes that the surface peaks are maximally displaced (about 4.5µm) in the lateral direction in the case of $\Delta\varphi = \frac{\pi}{2}$. This reveals the reason why the amplitude becomes minimal before $\Delta\varphi = \pi$

Due to the hydrodynamic pressure build-up, the surfaces' peaks are deformed in both normal and tangential directions and resulting in an additional phase shift due to tangential displacement of approximately $0.45\,\pi$ at $\Delta\varphi = \frac{\pi}{2}$; the real phase difference is $0.95\,\pi$, which leads asperities to be approximately in counterphase. In other words, for $\Delta\varphi = \frac{\pi}{2}$ and $\Delta\varphi = \pi$, higher pressures are exerted at the asperities' side surface; hence, the elastic deformation of surface features leads to an increment in film thickness and reduction of the pressure fluctuation in the contact.

Figure 14 shows a coefficient of friction which varies from 0.03 to 0.025, in which a local maximum of 0.03 is observed at $\Delta\varphi = 0$.

Finally, the temperature rise in the contact is seen to follow a similar trend, reaching a minimum around $\Delta\varphi = \frac{\pi}{2}$, corresponding to a reduction of 37% compared to the in-phase condition. The temperature rises as periodic asperities approach each other due to the decreased film thickness and increased shear rate. The maximum temperature varies between 339 K and 354 K in this period.

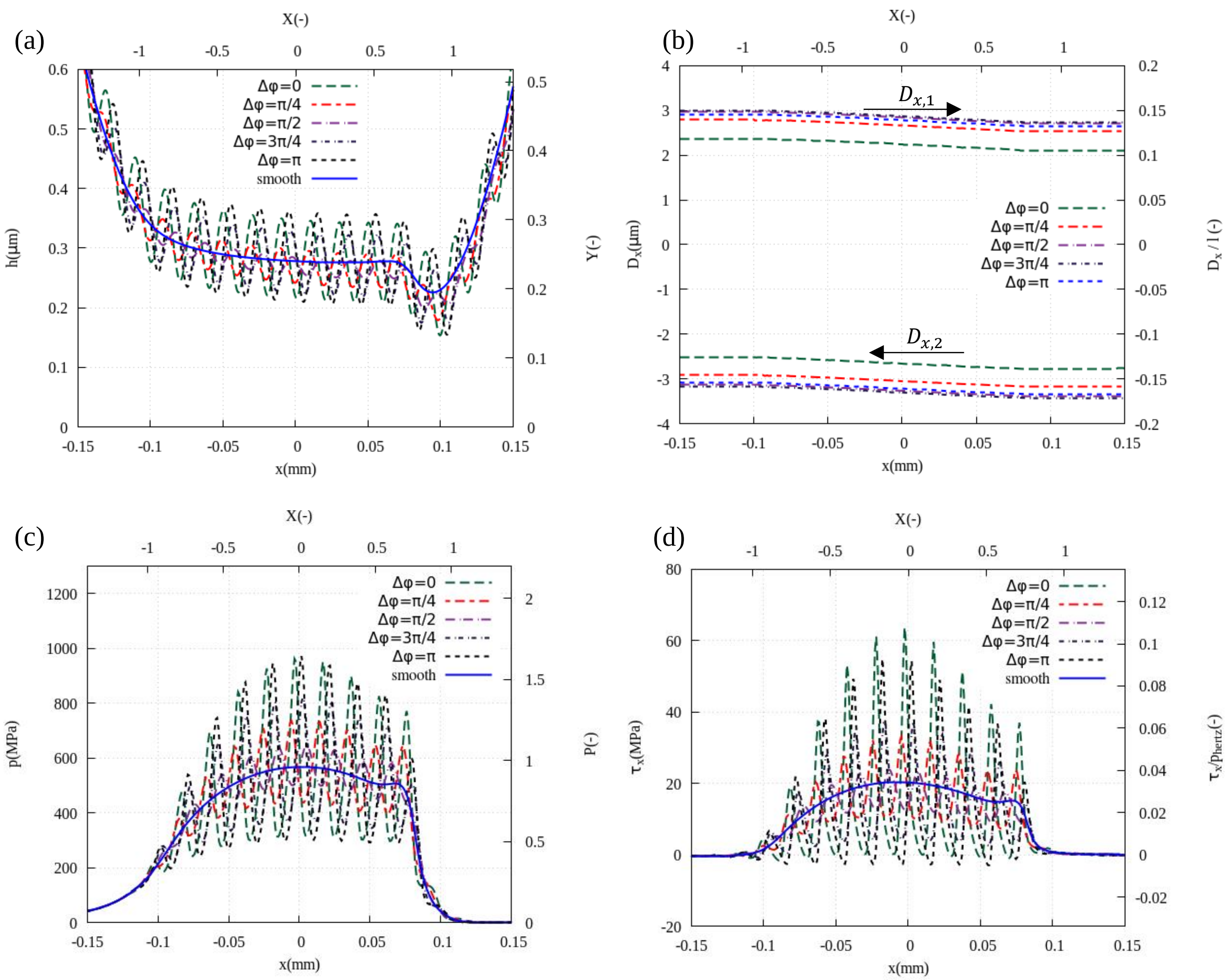

Figure 13 Effect of the phase difference (relative position) of surface asperities on a) film thickness, b) displacement of the upper surface ($D_{x,1}$) and lower surface ($D_{x,2}$) in flow direction

and c) pressure profile, and d) shear stress as a function of phase shift. $L = \frac{100\ \mathrm{kN}}{\mathrm{m}}, E_r = 345\ \mathrm{GPa}, \mathrm{SRR} = 1, l_1 = l_2 = 20\ \mu\mathrm{m}, A_1 = A_2 = 50\ \mathrm{nm}, \text{and}\ \varphi_1 = \frac{\pi}{2}$.

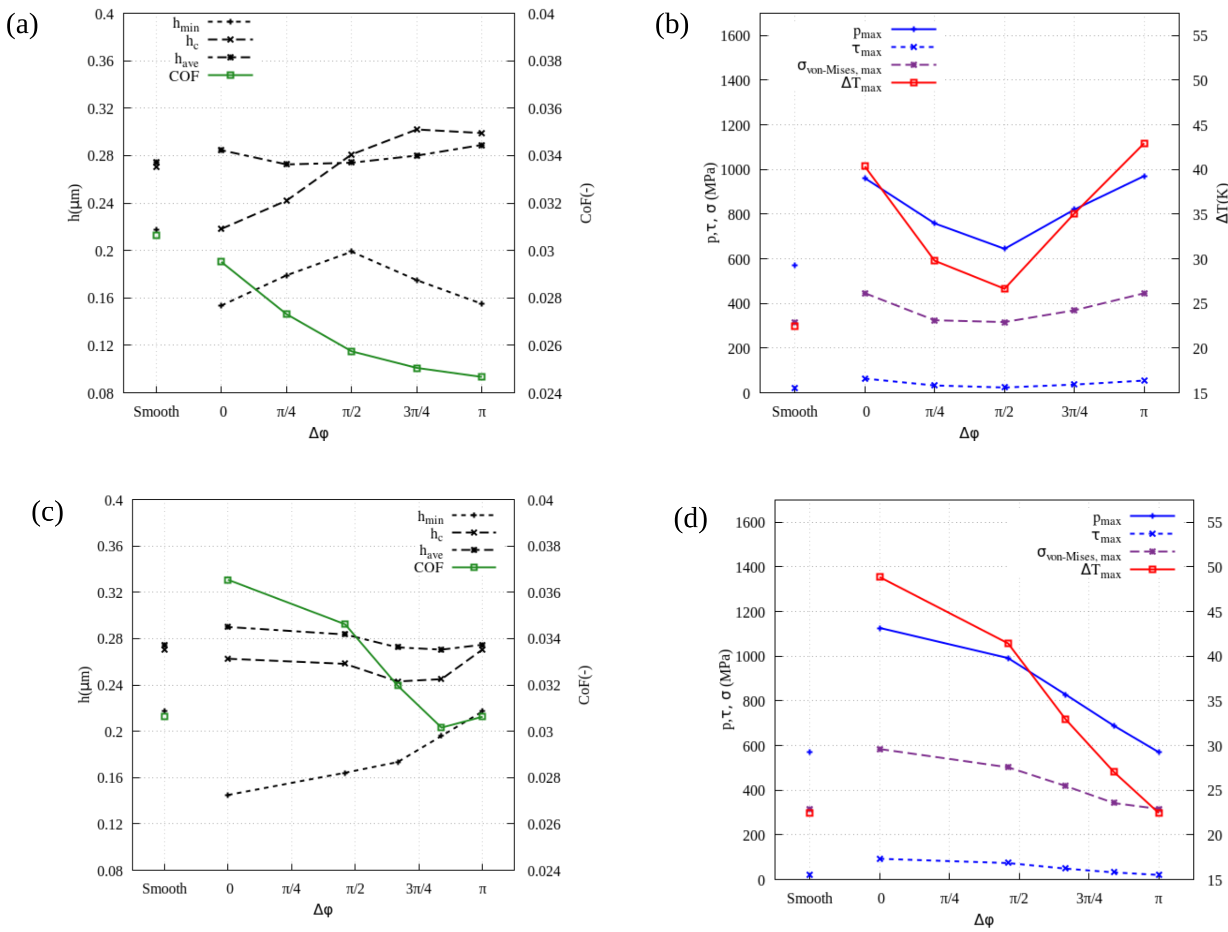

Figure 14 a) Minimum, central, average film thickness, and CoF, b) maximum pressure, shear stress, von Mises stress, and temperature rise as a function of phase-shift in the two-body method, c) and d) similar contact variables obtained by the equivalent body method.

It is clear that during the sliding motion of two cylinders with surface waviness, the film thickness is continuously varying due to oscillating pressure build-up when wave crests are passing each other, generating a pumping effect. This process is accompanied by temperature fluctuations within the contact as well as cyclic tangential deformations of the surface peaks, which creates an additional phase shift.

In the case of the equivalent body approach at $\Delta\varphi = \pi$, the surface is perfectly smooth (equation (38)), whereas for $\Delta\varphi = 0$ the waviness is equal to $A = 100$ nm and $l = 20$ μm. Hence, separate data has been generated for the equivalent body for $\Delta\varphi = 0 - \pi$ to map the results of the equivalent geometry in case of a phase shift. Figure 14 shows that the trends of the variables of interest are very different for the equivalent approach in comparison with the two-body approach. For example, the maximum contact pressure and temperature rise decrease continuously during one cycle. The temperature rise varies between $22 - 49$ K for the equivalent geometry, while it changes by $26 - 44$K in the two-body approach. Moreover, the maximum contact pressure has a 17% difference between both cases.

6. Conclusions

The effect of applying a wavy surface topology on the surfaces in Thermo-Elastohydrodynamic Lubrication (TEHL) has been investigated in this work using Computational Fluid Dynamics (CFD) and Fluid-Structure Interaction (FSI). A thorough assessment has been made of the often assumed apparent interchangeability between the equivalent reduced contact geometry using superimposed surface profiles and the more elaborate two-body contact geometry with a double-sided surface profile.

We considered a single-mode sinusoidal waviness profile superimposed on 1) the surface of the equivalent elastic cylindrical roller against a rigid smooth surface (i.e. equivalent approach) and 2) both surfaces individually (i.e. two-body approach). Thereto, a two-phase CFD model for TEHL of line contacts was developed in OpenFOAM and coupled with a linear elastic structural model for the solid deformation using a partitioned FSI approach. The code was validated and used to gain fundamental insight into the effects of the surface waviness on both the lubricant film and the solid bodies.

The main conclusions in this work can be summarised as follows

1. Using an equivalent wavy surface profile in equivalent single-body geometry with a half-space assumption, including the Carslaw-Jaeger thermal boundary condition, leads to an overestimated pressure, temperature, and von-Mises stress, whereas it yields an underestimation of the film thickness. The main reason is that the elastic deformations of the surface asperities of both bodies in the tangential direction are not taken into account. Moreover, the typically used Carslaw-Jaeger boundary condition, mimicking 2D heat transfer of moving surfaces, is shown not to be fully accurate. Generally, for the studied operating condition, up to 13% difference in minimum film thickness, 26% deviation in CoF, and up to 21% difference in maximum temperature rise and 17% maximum pressure have been observed for $SRR = 1$.
2. Under the conditions studied in this work, the minimum and central film thickness are seen to be smaller for wavy surfaces in comparison to smooth surfaces. Moreover, the minimum and central film thicknesses tend to decrease almost linearly with increasing waviness amplitude; they have been reduced by 38% and 27% for surface waves with 125 nm amplitude, respectively. However, the maximum values of pressure and temperature rise increase monotonously with increasing amplitude. Whereas the former rises up to 84%, the latter increases by 19% for surface waves with 125 nm amplitude. In contrast to the minimum and central film thickness, the average film thickness, reflecting the position of the nominal surface, increases slightly with increasing amplitude.
3. In the analysis of the influence of the phase difference for double-sided wavy textures, indications were found that the pressure and temperature oscillate during the rolling/sliding motion due to the cyclic pumping action of opposing wave crests which pass along each other. As a consequence, the minimum and central film thicknesses tend to oscillate with a magnitude of about 24% and 28% over one period, respectively. Due to a maximal tangential deformation of the opposing surface peaks in opposite directions, the minimum film thickness was not observed when the wave-crests were in counterphase ($\Delta\varphi = \pi$) but

when the wave-crests were lagging behind with about $\Delta\varphi = \frac{\pi}{2}$. Vastly different results were obtained when using the equivalent geometry in comparison with the two-body approach.

4. Using an equivalent body results in an underestimation of film thickness and an overestimation of pressure, temperature, and CoF when compared to the two-body approach for three different studied SRRs of 0, 1, and 2.
5. The high pressure peaks, which may rise up to twice the maximum Hertzian contact pressure, induce von Mises stresses in the solid material, which can be 68% higher than those in smooth surfaces. These maximum stress values are located very close to the surface, potentially altering the damage mechanism from subsurface to non-contact induced surface fatigue. This requires further investigations in future work.

Acknowledgements

This work is a part of the SBO project CONTACTLUB (‘S006519N’) granted by the Research Foundation - Flanders (FWO).

Appendix

Appendix A: Pressure equation

The pressure equation can be derived by a combination of momentum, continuity equation, and EoS of the mixture. If we employ equation (5), the temporal derivative of mixture density is calculated as [58]:

$$\frac{\partial \rho}{\partial t} = \frac{\partial \alpha}{\partial t}(\psi_v p - \rho_l) + (\alpha_v \psi_v + \alpha_l \psi_l)\frac{\partial p}{\partial t} + \alpha_v \frac{\partial \rho_v}{\partial T}\frac{\partial T}{\partial t} + \alpha_l \frac{\partial \rho_L}{\partial T}\frac{\partial T}{\partial t} \quad \text{(A. 1)}$$

The following pressure equation can be proved by inserting the temporal term in the mass conservation of fluid (equation (1)).

$$\frac{\partial(\psi p)}{\partial t} - \nabla \cdot \left(\rho \frac{1}{A} \nabla p\right) + \nabla \cdot \left(\rho \tilde{\tilde{u}}\right) + \nabla \cdot \left(\rho \frac{1}{A} \nabla p^{t-1}\right) + \frac{\partial \alpha}{\partial t}\left((\psi_v - \psi_l)p_{sat} - \rho_{l,0}\right) - p_{sat}\frac{\partial \psi}{\partial t} + \alpha_v \frac{\partial \rho_v}{\partial T}\frac{\partial T}{\partial t} + \alpha_l \frac{\partial \rho_L}{\partial T}\frac{\partial T}{\partial t} = 0 \quad \text{(A. 2)}$$

The pressure equation should be solved together with an equation of state for the mixture.

Appendix B: Energy equation

The model explained here is mainly developed by Hartinger et al. [52,53,58]; only some modifications have been made here to be compatible with the current study. The vapor enthalpy can be considered as below:

$$h_v = h_{0,v} + C_{p,v}(T - T_0) \quad \text{(B. 1)}$$

And for a compressible liquid, the enthalpy can be expressed as below:

$$h_l = h_{0,l} + \int_{T_0}^{T} C_{p,l} dT + \int_{P_0}^{P} \left(v - T \left(\frac{\partial v}{\partial T} \right)_P \right) dP \tag{B. 2}$$

where v is the specific volume of liquid ($v(P,T) = \frac{1}{\rho(P,T)}$). Equation (B. 2) is the complete form of liquid enthalpy. To achieve a complete energy equation for the mixture, the effect of temperature on the EoS should be incorporated. Therefore, the enthalpy of the liquid phase is re-written as follows:

$$h_l = h_{0,l} + \int_{T_0}^{T} C_{p,l} dT + \int_{P_0}^{P} \left(\frac{1}{\rho} (1 - \beta T) \right) dP \tag{B. 3}$$

$$\beta = \rho \left(\frac{\partial v}{\partial T} \right) = -\frac{1}{\rho} \left(\frac{\partial \rho}{\partial T} \right) \tag{B. 4}$$

where β is the thermal expansion coefficient. In addition, the heat of evaporation is as below:

$$h_{evap} = h_{0,v} - h_{0,l} \tag{B. 5}$$

Finally, the mixture enthalpy is defined as the volume averaged of phase enthalpy.

$$\rho h = \alpha_v \rho_v h_v + \alpha_l \rho_l h_l \tag{B. 6}$$

The energy equation can be arranged regarding the mixture enthalpy:

$$\frac{D(\rho h)}{Dt} = \nabla \cdot (k \nabla T) - \tau : \nabla \vec{u} + \frac{DP}{Dt} \tag{B. 7}$$

Equation (B. 7) can be expressed according to the fluid temperature by the combined equations (B. 1)-(B. 6):

$$\rho C_p \frac{DT}{Dt} + \frac{D\alpha_v}{Dt} (\rho_v h_v - \rho_l h_l) = \nabla \cdot (k \nabla T) - \tau : \nabla \vec{u} + \alpha_v \frac{DP}{Dt} + \alpha_l \beta T \frac{DP}{Dt} \tag{B. 8}$$

where the effective heat capacity and thermal conductivity of the mixture are defined as

$$\rho C_p = \alpha_v \rho_v C_{p,v} + \alpha_l \rho_l C_{p,l} \tag{B. 9}$$

$$k = \alpha_v k_v + \alpha_l k_l \tag{B. 10}$$

Appendix C: Scaling analysis

Scaling analysis for the fluid governing equation is beneficial to understand the time scale of this physics. Assuming a negligible convective term in equation (2) because of a very low Reynolds number, then each term can be estimated as follows:

$$\frac{\partial(\rho u)}{\partial t} + \nabla \cdot \tau = -\nabla \cdot p, \tag{C. 1}$$

$$\frac{\partial(\rho u)}{\partial t} \sim \frac{\rho U}{t_f} \tag{C. 2}$$

$$\nabla \cdot \tau \sim \frac{\mu U}{h_{ch}^2} \tag{C. 3}$$

$$\nabla \cdot p \sim \frac{P}{l_{ch}} \tag{C. 4}$$

The momentum equation can be written as:

$$\frac{\rho U}{t_f} \sim \frac{\mu U}{h_{ch}^2} + \frac{P}{l_{ch}} \tag{C. 5}$$

The time scale of fluid, t_f depends on the ratio of viscous forces to the pressure forces; also, the viscosity and speeds are important. The fluid time scale can be written based on viscous or pressure forces as follows:

$$t_f \sim \frac{\rho h_{ch}^2}{\mu} \tag{C. 6}$$

or

$$t_f \sim \frac{\rho U l_{ch}}{P} \tag{C. 7}$$

If the inlet viscosity and density values, maximum Hertz pressure, and half contact width are used, the fluid time scale of around $2ns$ and $0.34\ ns$ is obtained based on the viscous and pressure time scale.

On the other hand, the wave time period of asperity motion is $\frac{l}{U} \approx \frac{20 \mu\text{m}}{2.5\ \text{m/s}} \approx 8\ \mu\text{s}$, which is obviously several orders of magnitude greater than the fluid time scale. Hence, steady-state simulation of asperities motion in the contact is valid here based on this scale analysis.

References

[1] Almqvist A, Larsson R. The effect of two-sided roughness in rolling/sliding EHL line contacts. Tribol. Ser., vol. 43, Elsevier; 2003, p. 243–51.

[2] Hultqvist T, Vrcek A, Marklund P, Prakash B, Larsson R. Transient analysis of surface roughness features in thermal elastohydrodynamic contacts. Tribol Int 2020;141:105915.

[3] He T, Ren N, Zhu D, Wang J. Plasto-elastohydrodynamic lubrication in point contacts for surfaces with three-dimensional sinusoidal waviness and real machined roughness. J Tribol 2014;136.

[4] Hu Y-Z, Zhu D. A Full Numerical Solution to the Mixed Lubrication in Point Contacts. J Tribol 1999;122:1–9. https://doi.org/10.1115/1.555322.

[5] Kweh CC, Patching MJ, Evans HP, Snidle RW. Simulation of Elastohydrodynamic Contacts Between Rough Surfaces. J Tribol 1992;114:412–9. https://doi.org/10.1115/1.2920900.

[6] Lubrecht AA, Ten Napel WE, Bosma R. The Influence of Longitudinal and Transverse Roughness on the Elastohydrodynamic Lubrication of Circular Contacts. J Tribol 1988;110:421–6. https://doi.org/10.1115/1.3261645.

[7] Liu M, Wu C, Yan C. Predicting fatigue life for finite roller contacts based on a mixed

EHL model using realistic surface roughness. J Mech Sci Technol 2017;31:3419–28.

[8] Ren N, Zhu D, Chen WW, Liu Y, Wang QJ. A Three-Dimensional Deterministic Model for Rough Surface Line-Contact EHL Problems. J Tribol 2008;131. https://doi.org/10.1115/1.2991291.

[9] Venner CH, ten Napel WE. Surface Roughness Effects in an EHL Line Contact. J Tribol 1992;114:616–22. https://doi.org/10.1115/1.2920926.

[10] Zhu D, Ai X. Point Contact EHL Based on Optically Measured Three-Dimensional Rough Surfaces. J Tribol 1997;119:375–84. https://doi.org/10.1115/1.2833498.

[11] Kim TW, Cho YJ. The Flow Factors Considering the Elastic Deformation for the Rough Surface with a Non-Gaussian Height Distribution. Tribol Trans 2008;51:213–20. https://doi.org/10.1080/10402000701730502.

[12] Morales-Espejel GE. Flow factors for non-Gaussian roughness in hydrodynamic lubrication: An analytical interpolation. Proc Inst Mech Eng Part C J Mech Eng Sci 2009;223:1433–41.

[13] Pei J, Han X, Tao Y, Feng S. Mixed elastohydrodynamic lubrication analysis of line contact with Non-Gaussian surface roughness. Tribol Int 2020:106449.

[14] Yan X-L, Wang X-L, Zhang Y-Y. Influence of Roughness Parameters Skewness and Kurtosis on Fatigue Life Under Mixed Elastohydrodynamic Lubrication Point Contacts. J Tribol 2014;136. https://doi.org/10.1115/1.4027480.

[15] Allen Q, Raeymaekers B. Maximizing the Lubricant Film Thickness Between a Rigid Microtextured and a Smooth Deformable Surface in Relative Motion, Using a Soft Elasto-Hydrodynamic Lubrication Model. J Tribol 2020;142.

[16] Hooke CJ, Morales-Espejel GE. Rapid analysis of low-amplitude sinusoidal roughness in rolling-sliding elastohydrodynamic contacts including thermal effects. Proc Inst Mech Eng Part C J Mech Eng Sci 2018;232:1690–706.

[17] Hooke CJ, Morales-Espejel GE. Analysis of general low-amplitude roughness in rolling–sliding elastohydrodynamic contacts including thermal effects. Proc Inst Mech Eng Part J J Eng Tribol 2019;233:1648–60.

[18] Hultqvist T, Vrček A, Marklund P, Larsson R. On Waviness and Two-Sided Surface Features in Thermal Elastohydrodynamically Lubricated Line Contacts. Lubricants 2020;8:64.

[19] Kaneta M, Matsuda K, Wang J, Cui J, Yang P, Nishikawa H, et al. Numerical Study on the Interaction of Transverse and Longitudinal Roughness on Elastohydrodynamic Lubrication Contact Surfaces With Different Thermal Conductivities and Elastic Moduli. J Tribol 2021;143.

[20] Kaneta M, Matsuda K, Wang J, Yang P. Numerical Study on Effect of Dimples on Tribo-Characteristics in Non-Newtonian Thermal Elastohydrodynamic Lubrication Point Contacts With Different Mechanical and Thermal Properties. J Tribol 2020;142.

[21] Kaneta M, Matsuda K, Wang J, Yang P. Numerical Study on Effect of Thermal Conductivity in Point Contacts with Longitudinal Roughness on Abnormal Pressure

Distribution. J Tribol n.d.:1–27.

[22] Chimanpure AS, Kahraman A, Talbot D. A Transient Mixed Elastohydrodynamic Lubrication Model for Helical Gear Contacts. J Tribol 2021;143.

[23] Everitt C-M, Alfredsson B. The influence of gear surface roughness on rolling contact fatigue under thermal elastohydrodynamic lubrication with slip. Tribol Int 2020;151:106394. https://doi.org/https://doi.org/10.1016/j.triboint.2020.106394.

[24] Everitt C-M, Vrček A, Alfredsson B. Experimental and numerical investigation of asperities and indents with respect to rolling contact fatigue. Tribol Int 2020;151:106494.

[25] Marian M, Grützmacher P, Rosenkranz A, Tremmel S, Mücklich F, Wartzack S. Designing surface textures for EHL point-contacts - Transient 3D simulations, meta-modeling and experimental validation. Tribol Int 2019;137:152–63. https://doi.org/https://doi.org/10.1016/j.triboint.2019.03.052.

[26] Xu G, Sadeghi F. Thermal EHL Analysis of Circular Contacts With Measured Surface Roughness. J Tribol 1996;118:473–82. https://doi.org/10.1115/1.2831560.

[27] Yang Y, Li W, Wang J, Zhou Q. On the mixed EHL characteristics, friction and flash temperature in helical gears with consideration of 3D surface roughness. Ind Lubr Tribol 2019.

[28] Shi X-J, Wang L-Q, Qin F-Q. Non-Gaussian surface parameters effects on Micro-TEHL performance and surface stress of aero-engine main-shaft ball bearing. Tribol Int 2016;96:163–72.

[29] Zhao J-J, Lin M-X, Song X-C, Wei N. Coupling analysis of the fatigue life and the TEHL contact behavior of ball screw under the multidirectional load. Ind Lubr Tribol 2020.

[30] Masjedi M, Khonsari MM. Theoretical and experimental investigation of traction coefficient in line-contact EHL of rough surfaces. Tribol Int 2014;70:179–89.

[31] Meng FM, Qin DT, Chen HB, Hu YZ, Wang H. Study on combined influence of inter-asperity cavitation and elastic deformation of non-Gaussian surfaces on flow factors. Proc Inst Mech Eng Part C J Mech Eng Sci 2008;222:1039–48.

[32] Wang X, Liu Y, Zhu D. Numerical solution of mixed thermal elastohydrodynamic lubrication in point contacts with three-dimensional surface roughness. J Tribol 2017;139.

[33] Gu C, Meng X, Xie Y, Fan J. A thermal mixed lubrication model to study the textured ring/liner conjunction. Tribol Int 2016;101:178–93.

[34] Srirattayawong S, Gao S. A computational fluid dynamics study of elastohydrodynamic lubrication line contact problem with consideration of surface roughness. Comput Therm Sci An Int J 2013;5.

[35] Hajishafiee A. Finite-volume CFD modelling of fluid-solid interaction in EHL contacts. Imperial College, 2013.

[36] Patir N, Cheng HS. An average flow model for determining effects of three-dimensional roughness on partial hydrodynamic lubrication 1978.

[37] Hooke CJ. Roughness in rolling-sliding elastohydrodynamic lubricated contacts. Proc Inst

Mech Eng Part J J Eng Tribol 2006;220:259–71.

[38] Morales-Espejel GE. Surface roughness effects in elastohydrodynamic lubrication: A review with contributions. Proc Inst Mech Eng Part J J Eng Tribol 2014;228:1217–42. https://doi.org/10.1177/1350650113513572.

[39] Hooke CJ. The behaviour of low-amplitude surface roughness under line contacts: non-Newtonian fluids. Proc Inst Mech Eng Part J J Eng Tribol 2000;214:253–65.

[40] Hooke CJ. Surface roughness modification in elastohydrodynamic line contacts operating in the elastic piezoviscous regime. Proc Inst Mech Eng Part J J Eng Tribol 1998;212:145–62.

[41] Hooke CJ. The behaviour of low-amplitude surface roughness under line contacts. Proc Inst Mech Eng Part J J Eng Tribol 1999;213:275–85.

[42] Habchi W. On roughness attenuation in elastohydrodynamic lubricated line and circular contacts. Proc Inst Mech Eng Part J J Eng Tribol 2022:13506501221137972.

[43] Conry TF. Thermal Effects on Traction in EHD Lubrication. J Lubr Technol 1981;103:533–8. https://doi.org/10.1115/1.3251732.

[44] Habchi W. A full-system finite element approach to elastohydrodynamic lubrication problems: application to ultra-low-viscosity fluids. Univ Lyon Fr 2008.

[45] Schäfer CT, Giese P, Rowe WB, Woolley NH. Elastohydrodynamically lubricated line contact based on the Navier-Stokes equations. Tribol. Ser., vol. 38, Elsevier; 2000, p. 57–69.

[46] Scurria L, Tamarozzi T, Voronkov O, Fauconnier D. Quantitative Analysis of Reynolds and Navier–Stokes Based Modeling Approaches for Isothermal Newtonian Elastohydrodynamic Lubrication. J Tribol 2021;143. https://doi.org/10.1115/1.4050272.

[47] Dowson D. A generalized Reynolds equation for fluid-film lubrication. Int J Mech Sci 1962;4:159–70. https://doi.org/10.1016/S0020-7403(62)80038-1.

[48] Peiran Y, Shizhu W. A generalized Reynolds equation for non-Newtonian thermal elastohydrodynamic lubrication 1990.

[49] Almqvist T, Larsson R. The Navier–Stokes approach for thermal EHL line contact solutions. Tribol Int 2002;35:163–70.

[50] Rajagopal KR, Szeri AZ. On an inconsistency in the derivation of the equations of elastohydrodynamic lubrication. Proc R Soc A Math Phys Eng Sci 2003;459:2771–86. https://doi.org/10.1098/rspa.2003.1145.

[51] Hao L, Meng Y. Comparisons of TEHL Simulations of Newtonian Fluids in Line Contacts between the 3D FEM and the Reynolds Equation–Based Approaches*. Tribol Trans 2016;59:641–54. https://doi.org/10.1080/10402004.2015.1100769.

[52] Hartinger M, Dumont M-L, Ioannides S, Gosman D, Spikes H. CFD modeling of a thermal and shear-thinning elastohydrodynamic line contact. J Tribol 2008;130:41503.

[53] Hartinger M, Reddyhoff T. CFD modeling compared to temperature and friction measurements of an EHL line contact. Tribol Int 2018;126:144–52.

[54] Hajishafiee A, Kadiric A, Ioannides S, Dini D. A coupled finite-volume CFD solver for two-dimensional elasto-hydrodynamic lubrication problems with particular application to rolling element bearings. Tribol Int 2017;109:258–73.

[55] Bruyere V, Fillot N, Morales-Espejel GE, Vergne P. Computational fluid dynamics and full elasticity model for sliding line thermal elastohydrodynamic contacts. Tribol Int 2012;46:3–13. https://doi.org/10.1016/j.triboint.2011.04.013.

[56] Kärrholm FP. Numerical modelling of diesel spray injection, turbulence interaction and combustion. Chalmers University of Technology Gothenburg, Sweden; 2008.

[57] Chung M-S, Park S-B, Lee H-K. Sound speed criterion for two-phase critical flow. J Sound Vib 2004;276:13–26.

[58] Hartinger M. CFD modelling of elastohydrodynamic lubrication 2007.

[59] Hajishafiee A. Finite-volume CFD modelling of fluid-solid interaction in EHL contacts. Imperial College London, 2013.

[60] Kim HJ, Ehret P, Dowson D, Taylor CM. Thermal elastohydrodynamic analysis of circular contacts part 2: Non-Newtonian model. Proc Inst Mech Eng Part J J Eng Tribol 2001;215:353–62.

[61] Kim HJ, Ehret P, Dowson D, Taylor CM. Thermal elastohydrodynamic analysis of circular contacts part 1: Newtonian model. Proc Inst Mech Eng Part J J Eng Tribol 2001;215:339–52.

[62] Bair SS. High pressure rheology for quantitative elastohydrodynamics. Elsevier; 2019.

[63] Bair S, Liu Y, Wang QJ. The pressure-viscosity coefficient for Newtonian EHL film thickness with general piezoviscous response 2006.

[64] Habchi W, Vergne P, Bair S, Andersson O, Eyheramendy D, Morales-Espejel GE. Influence of pressure and temperature dependence of thermal properties of a lubricant on the behaviour of circular TEHD contacts. Tribol Int 2010;43:1842–50.

[65] Gecim B, Winer WO. Lubricant limiting shear stress effect on EHD film thickness 1980.

[66] Cardiff P, Karač A, De Jaeger P, Jasak H, Nagy J, Ivanković A, et al. An open-source finite volume toolbox for solid mechanics and fluid-solid interaction simulations. ArXiv Prepr ArXiv180810736 2018.

[67] Tuković Ž, Karač A, Cardiff P, Jasak H, Ivanković A. OpenFOAM finite volume solver for fluid-solid interaction. Trans FAMENA 2018;42:1–31.

[68] Cardiff P, Karač A, De Jaeger P, Jasak H, Nagy J, Ivanković A, et al. An open-source finite volume toolbox for solid mechanics and fluid-solid interaction simulations. ArXiv Prepr ArXiv180810736 2018.

[69] Degroote J, Bathe K-J, Vierendeels J. Performance of a new partitioned procedure versus a monolithic procedure in fluid–structure interaction. Comput Struct 2009;87:793–801.

[70] Degroote J. Partitioned simulation of fluid-structure interaction. Arch Comput Methods Eng 2013;20:185–238.

[71] Tošić M. Model of Thermal EHL Based on Navier-Stokes Equations: Effects of Asperities and Extreme Loads 2019.

[72] Tošić M, Larsson R, Jovanović J, Lohner T, Björling M, Stahl K. A Computational Fluid Dynamics Study on Shearing Mechanisms in Thermal Elastohydrodynamic Line Contacts. Lubricants 2019;7:69.

[73] Srirattayawong S. CFD study of surface roughness effects on the thermo-elastohydrodynamic lubrication line contact problem 2014.

[74] Tošić M, Larsson R, Jovanović J, Lohner T, Björling M, Stahl K. A Computational Fluid Dynamics Study on Shearing Mechanisms in Thermal Elastohydrodynamic Line Contacts. Lubricants 2019;7:69. https://doi.org/10.3390/lubricants7080069.

[75] Bair S. Reference liquids for quantitative elastohydrodynamics: selection and rheological characterization. Tribol Lett 2006;22:197–206.

[76] Björling M, Habchi W, Bair S, Larsson R, Marklund P. Friction reduction in elastohydrodynamic contacts by thin-layer thermal insulation. Tribol Lett 2014;53:477–86.

[77] Singh K, Sadeghi F, Peterson W, Lorenz SJ, Villarreal J, Jinmon T. A CFD-FEM based partitioned fluid structure interaction model to investigate surface cracks in elastohydrodynamic lubricated line contacts. Tribol Int 2022;171:107532.

[78] Habchi W, Bair S. The role of the thermal conductivity of steel in quantitative elastohydrodynamic friction. Tribol Int 2020;142:105970.

[79] Zhu D, Ren N, Wang QJ. Pitting life prediction based on a 3D line contact mixed EHL analysis and subsurface von Mises stress calculation 2009.

[80] Venner CH, Lubrecht AA. Numerical Simulation of a Transverse Ridge in a Circular EHL Contact Under Rolling/Sliding. J Tribol 1994;116:751–61. https://doi.org/10.1115/1.2927329.